

**DESIGN AND ANALYSIS OF A HIGHLY SENSITIVE SURFACE
PLASMON RESONANCE REFRACTIVE INDEX MULTI-
CHANNEL SENSOR FOR MULTI-ANALYTE SENSING IN
VISIBLE TO NEAR-INFRARED REGION**

A thesis submitted to
the Department of Electrical & Electronic Engineering
of
Bangladesh University of Engineering & Technology
in partial fulfillment of the requirements
for the degree of
**Master of Science in
Electrical & Electronic Engineering**
by

K M Mustafizur Rahman: 1018062273

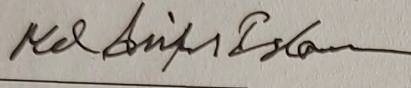


Department of Electrical and Electronic Engineering (EEE)
BANGLADESH UNIVERSITY OF ENGINEERING AND TECHNOLOGY (BUET)
13 December, 2021

Approval Certificate

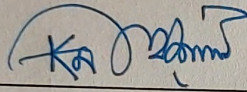
The thesis titled “**Design and Analysis of a Highly Sensitive Surface Plasmon Resonance Refractive Index Multi-channel Sensor for Multi-analyte Sensing in Visible to Near-infrared Region**” submitted by K M Mustafizur Rahman, Roll No.: 1018062273, Session: October 2018, has been accepted as satisfactory in partial fulfilment of the requirement for the degree of Master of Science in Electrical and Electronic Engineering on 13/12/2021.

BOARD OF EXAMINERS



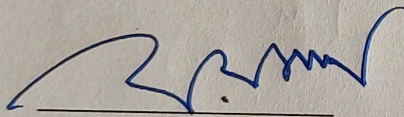
1. Dr. Md. Asiful Islam
Associate Professor
Department of EEE, BUET, Dhaka

Chairman
(Supervisor)



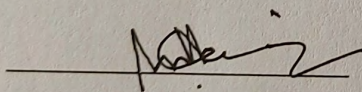
2. Dr. Md. Kamrul Hasan
Professor & Head
Department of EEE, BUET, Dhaka

Member
(Ex- officio)



3. Dr. Mohammad Faisal
Professor
Department of EEE, BUET, Dhaka

Member

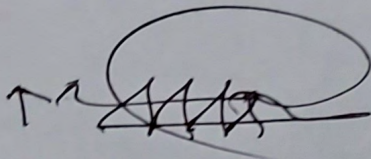


4. Dr. M. Mofazzal Hossain
Professor & Head
Department of EEE, University of
Liberal Arts Bangladesh (ULAB)

Member
(External)

CANDIDATE'S DECLARATION

This is to certify that the work entitled “**Design and Analysis of a Highly Sensitive Surface Plasmon Resonance Refractive Index Multi-channel Sensor for Multi-analyte Sensing in Visible to Near-infrared Region**” is the outcome of research carried out by me under the supervision of Dr. Md. Asiful Islam. It is hereby declared that this thesis/project or any part of it has not been submitted elsewhere for the award of any degree or diploma.



K M Mustafizur Rahman

Student ID: 1018062273

DEDICATION

To my dearest Parents

Table of Contents

Declaration	...iii
Table of Contents	...v
List of Figures	...ix
List of Tables	...xii
List of Abbreviations of Technical Symbols and Terms	...xiii
Acknowledgements	...xv
Abstract	...xvi
Chapter 1:	...01
Introduction	
1.1 Motivation	...01
1.2 Objectives	...02
1.3 Possible Outcome	...02
1.4 Methodology	...03
1.5 Thesis Outline	...04
Chapter 2:	...06
Literature Study	
2.1 Photonic Crystal Fiber and Surface Plasmon Resonance	...06
2.1.1 Photonic Crystal Fiber	...06
2.1.1.1 History of PCF	...07

2.1.1.2	Light Guiding Mechanism Through Fiber	...07
2.1.1.3	Light Guiding Mechanism Through PCF	...8
2.1.2	Surface Plasmon Resonance	...08
2.1.2.1	SPR Basis	...08
2.1.2.2	Excitation of SPR	...09
2.1.2.2.1	Otto Configuration	...10
2.1.2.2.2	Kretschmann Configuration	...10
2.1.2.3	Sensing Principle	...11
2.1.2.4	Photonic Crystal Fiber Based SPR Sensor	...11
2.1.2.5	Application of SPR Based Sensor	...11
2.2	Literature Review	...12
2.3	Summary	...13
	Chapter 3:	...14
	Sensor Related Theory and Step by Step Design	
3.1	Sensor Related Theory	...14
3.2	Step by Step Design Topology	...18
3.3	Simulation Setup	...21
3.4	Summary	...21
	Chapter 4:	...22
	Sensor's Basic Structure Optimization	
4.1	Pitch Optimization	...22
4.2	Optimization of Air-holes (d_1 and d_2)	...23

4.3	Au Thickness Layer (t_{Au}) Optimization	...24
4.4	Optimization of Distances between Adjacent Air-holes (d_3)	...25
4.5	Summary	...26
Chapter 5:		...27
Multi-channel Optimization		
5.1	Preferred State of Polarization and SPP Mode Selection	...27
5.2	Optimization of Channel-1(With Au)	...30
5.3	Optimization Inter-channel Gap (d_g)	...31
5.4	Optimization of Channel-2 (With Au and Ta_2O_5)	...32
5.5	Optimization of Channel-3 (With Au and TiO_2)	...33
5.6	Summary	...33
Chapter 6:		...34
Result and Discussion		
6.1	Optimized Parameters	...34
6.2	Phase-matching and Dispersion Curve Analysis	...34
6.3	CL Analysis	...36
6.4	Wavelength Sensitivity Analysis	...36
6.5	Amplitude Sensitivity Analysis	...38
6.6	Sensor Resolution	...39
6.7	FOM Analysis	...40
6.8	Summary of Important Data	...40
6.9	Polynomial Fitting Curve	...41

6.10	Performance Comparison	...42
6.11	Working Principle of the Proposed Sensor	...44
6.12	Summary	...44
Chapter 7:		...45
Sensor's Application		
7.1	Probable Application of the Proposed Sensor	...45
7.2	Specific Application - Cancerous Cell Detection	...46
7.3	Summary	...47
Chapter 8:		...48
Fabrication Feasibility of the Sensor		
8.1	Fabrication Tolerance Test	...48
8.2	Fabrication Steps of the Proposed Sensor	...49
8.3	Summary	...50
Chapter 9:		...51
Conclusion and Future Works		
9.1	Conclusion	...51
9.2	Scope of the Future Work	...52
List of Author's Publication		...53
References		...54

List of Figures

Fig No.	Description	Page
Fig. 2.1	(a) to (d) Schematic Diagram of PCF with different lattice configuration	...6
Fig. 2.2	TIR principle in guiding light through fiber	...7
Fig. 2.3	(a) Microscopic image of solid-core PCF (b) Microscopic image of hollow-core PCF (c) Light guiding mechanism in solid-core PCF with modified TIR (d) Light guiding mechanism in hollow-core PCF with bandgap effect.	...8
Fig. 2.4	Surface plasmon polariton (SPP) excitation method (a) Otto configuration. (b) Kretschmann configuration	...10
Fig. 3.1	Step-by-step design procedure of the proposed sensor. (a) Truncating a regular PCF with core (b) Corresponding loss spectra of the sensor with the structure shown in (a). (c) and (d) Modified structure and Corresponding CL spectra as per new design	...18
Fig. 3.2	The proposed multi-channel Sensor's cross-section schematic, demonstrating several geometric parameters.	...20
Fig. 3.3	Electromagnetic field distribution. (a-b) y-polarized core guided and SPP modes for $n_a = 1.41$ in channel-1 (c-d) y-polarized core guided and SPP modes for $n_a = 1.41$ in channel-2 (e-f) x-polarized core guided and SPP modes for $n_a = 1.41$ in channel-3.	...21
Fig. 4.1	Pitch variation effect on the basic structure. CL spectra for pitch, $\Lambda = 1.8, 2.0,$ and $2.2 \mu\text{m}$ for RI of 1.41-1.42.	...22
Fig. 4.2	Variation of Au layer thickness on the reference structure. (a) CL spectra for $t_{\text{Au}} = 45 \text{ nm}$ for RI range of 1.38-1.42. (b) CL spectra for $t_{\text{Au}} = 50 \text{ nm}$...24

for RI range of 1.37-1.42. (c) CL spectra for $t_{Au} = 55$ nm for RI range of 1.37-1.42. (d) CL spectra for $t_{Au} = 60$ nm for RI range of 1.38-1.41.

Fig. 4.3	Effect of variation of distance between adjacent air-holes, d_3 . Plot showing CL spectra for $d_3 = 1.5, 2.0$ and $2.5 \mu\text{m}$ for RI of 1.41-1.42	...25
Fig. 5.1	State of polarization (x and y) and associated loss spectra. (a) – (c) CL spectra for $n_a = 1.41$ for channel-1, 2 and 3 respectively.	...28
Fig. 5.2	SPP modes analysis. (a) SPP-1 mode. (b) SPP-2 mode. (c) SPP-3 mode. (d) Interaction of y-polarized core mode with different SPP modes.	...29
Fig. 5.3	Variation of Au layer thickness, t_{Au} in the channel-1 of the proposed multi-channel and multi-analyte sensor.	...30
Fig. 6.1	Sensor's wavelength-dependent dispersion relation for SPP mode and core-guided mode, for $n_a = 1.41$. (a) Channel-1 with y-polarization. (b) Channel-2 with y-polarization. (c) Channel-3 with x-polarization	...35
Fig. 6.2	CL plots for the optimized sensor. (a) Channel-1. (b) Channel-2. (c) Channel-3 for RI of 1.41-1.42	...37
Fig. 6.3	AS spectra for the optimized sensor. (a) Channel-1. (b) Channel-2. (c) Channel-3 for RI of 1.41-1.42	...38
Fig. 6.4	Polynomial curve fitting. (a) For channel-1 (b) For channel-2 (c) For channel-3	...41
Fig. 7.1	CL and AS spectra for the cancerous cell detection. (a) CL plots for healthy and cancerous Jurkat and PC-12 cell in Channel-1. (b) CL plots for healthy and cancerous MCF-7 and MDA-MB-23 cell in Channel-2 (c) CL plots for healthy and cancerous Basal and HeLa cell in Channel-3. (d) AS plots for PC-12, Jurkat, MCF-7, MDA-MB-23, Basal and HeLa cells.	...47

- Fig. 8.1 CL loss profile for -5% to +5 % variation in structural parameters such as, ...48
d₁,d_g,Λ,d₂ and t_{Au} for RI of 1.41 in channel-1. In addition, loss curve
(red color) is shown for RI of 1.41 of proposed sensor for channel-1.
- Fig. 8.2 Illustrations showing step-by-step stack-and-draw method for fabricating ...49
proposed multi-analyte and multi-channel sensor.

List of Tables

Table No.	Description	Page
Table 4.1	Air-holes Diameter (d_1 and d_2) Variation Effect	...23
Table 5.1	Performance Parameters for Varying Au Layer Thickness	...31
Table 5.2	Performance Parameter as a Result of Varying Inter Channel Gap (d_g)	...31
Table 5.3	Performance Parameters as a Result of Varying Au and Ta_2O_5 Layer Thicknesses	...32
Table 5.4	Performance Parameters as a Result of Varying Au and TiO_2 Layer Thicknesses	...34
Table 6.1	Summary of Sensor's Performance in Three Channels	...40
Table 6.2	Comparative Performance Analysis of Proposed Sensor	...43
Table 7.1	RI (1.36-1.42) of different Analytes For Multi-Channel Sensor	...45
Table 7.2	Performance of the sensor in diagnosing cancerous cells of human body	...46

List of Abbreviations of Technical Symbols and Terms

Abbreviation/symbol	Meaning
Au	Gold
AS	Amplitude Sensitivity
CL	Confinement Loss
cm	Centimetre
d_1	Diameter of larger air-hole
d_2	Diameter of smaller air-hole
d_3	Distance between adjacent air-holes
dB	Decibel
d_g	Inter-channel gap
FEM	Finite Element Method
FOM	Figure of Merit
FWHM	Full Width at Half Maximum
Im	Imaginary
n_{eff}	Effective Refractive Index
nm	Nano Meter
OTS	Optical Tunable Source
PCF	Photonic Crystal Fiber
PML	Perfectly Matched Layer
RI	Refractive Index
RIU	Refractive Index Unit
s_λ	Wavelength Sensitivity in nm/RIU
SMF	Single-mode Fiber
SPP	Surface Plasmon Polariton
SPP-1	First-order SPP Mode
SPP-2	Second-order SPP Mode
SPP-3	Third-order SPP Mode
SPR	Surface Plasmon Resonance
t_{Au}	Thickness of Au layer

$t_{\text{Ta}_2\text{O}_5}$	Thickness of Ta_2O_5 layer
Ta_2O_5	Tantalum Pentoxide
t_{TiO_2}	Thickness of TiO_2 Layer
TiO_2	Titanium Dioxide
TIR	Total Internal Reflection
WS	Wavelength Sensitivity
Λ	Pitch
Δn_a	Variation between two Adjacent n_a
$\Delta\lambda_{peak}$	Wavelength peak shift in nm
$\Delta\lambda_{min}$	Minimum spectral resolution
$\alpha(\lambda, n_a)$	CL value for any n_a at specified λ
$\partial\alpha(\lambda, n_a)$	CL difference for a specified λ between two adjacent analyte RIs
∂n_a	Difference between two adjacent analytes RI.
ϵ_{Au}	Permittivity of Au
ϵ_∞	Permittivity at high frequency, 5.9673
ω	Angular frequency, $2\pi\nu/\lambda$
v	The velocity of light, 3×10^8 m/s
ω_D	Plasma frequency, $\omega_D/2\pi = 2113.6$ THz
γ_D	Damping frequency, $\gamma_D/2\pi = 15.92$ THz
$\Delta\epsilon$	Weighting factor, 1.09
$\Omega_L/2\pi$	Oscillator strength, 650.07 THz
$\Gamma_L/2\pi$	Spectral width, 104.86 THz
π	Pi (3.1416)
λ	Wavelength in nm
μm	Micro meter

Acknowledgement

At first I would like to remember ALLAH, the Almighty with due respect. I want to thank the almighty ALLAH for giving me the opportunity to conduct my thesis. It becomes possible to reach the destination because of His grace and mercy. It is a great pleasure for me to express unfettered gratification, sincere appreciation and profound respect to my supervisor Dr. Md. Asiful Islam, Associate, Professor, Department of Electrical and Electronic Engineering, Bangladesh University of Engineering and Technology, Bangladesh, for his constructive suggestion, scholastic guidance, constant inspiration, and kind co-operation throughout the entire progress of this thesis work. It would have been impossible for me to accomplish my work without his remarkable advices.

I want to take the opportunity to cordially thank Dr. M Shah Alam, Professor, Department of Electrical and Electronic Engineering, Bangladesh University of Engineering and Technology, Bangladesh for correcting me by giving his valueable advices. I would also like to thank all of my course-work faculties of Department of Electrical and Electronic Engineering, Bangladesh University of Engineering and Technology, Bangladesh.

I extend my gratitude and appreciation to my respected and beloved parents as well as my wife for their cooperation, patience and faith on me to complete my thesis successfully. Finally, I wish to thank all the concerned teachers and staffs and my respected group members of the department for their direct and indirect assistance at different events of the work.

Abstract

Photonic crystal fiber (PCF) based surface plasmon resonance (SPR) sensors have a unique sensing capability and can be applied over a wide refractive index (RI) range. In this research work a simple yet highly sensitive multi-channel hexagonal PCF based SPR RI sensor for detecting multiple analytes has been put forwarded. The target analytes and the plasmonic materials, such as, gold (Au), Au with Tantalum Pentoxide (Ta_2O_5) and Au with Titanium Dioxide (TiO_2) are employed around the exterior of the sensor for the feasibility of the operation. Twelve circular air-holes in two layers constitute the PCF structure which makes the fabrication process easy and realizable. Numerical investigations are carried out employing a full-vector finite element method (FEM) of COMSOL Multiphysics to obtain the sensing performance of the PCF-SPR structure. After optimizing the structural parameters, the sensor achieves maximum wavelength sensitivity (WS) of 38100 and 21600 nm/RIU, for channels-1 and 2, respectively. For channel-3, the sensor achieves a maximum WS of 45800 nm/RIU. To the best of our knowledge, the proposed sensor achieves better performance in terms of wavelength sensitivity, wavelength resolution, amplitude sensitivity, amplitude resolution, figure of merit, etc., compared to the existing literature. Overall, the sensor achieves RI range of 1.36 to 1.42 and within which many analytes samples fall. As a specific application, this multi-channel sensor may be employed to detect cancerous cells. In the case of cancerous cell detection, the proposed sensor achieves maximum WS and amplitude sensitivity of 12000 nm/RIU and $-2440.30 \text{ RIU}^{-1}$, respectively, for HeLa cells. It is envisaged that the proposed sensor has a high potential to detect unknown RI for different chemical and biomedical applications due to its superior performance, simple design, and multi-analyte detection ability.

Chapter 1

Introduction

1.1 Motivation

Surface plasmon (SP) is the quanta of oscillations of surface charges produced by the electric field in the boundary of dielectric and metal surfaces. SPR is an electro-optical activity that provides real-time observation for the binding interactions between biomolecule and analyte. SPR sensors have a unique sensing capability and can be applied over a wide RI range. SPR sensor also offers advantages such as nano/micro size, easy light launching, different modes-multiplexing capabilities, evanescent field penetration controlling ability, etc. SPR sensor covers a broad range of applications such as bioimaging, environmental monitoring, organic chemical sensing, telemedicine, colorimetric sensing, food analysis, clinical diagnostics, bioaffinity studies, drug development. Based on the position of the analyte in the sensor structure, there are two types of PCF-SPR sensing methods; firstly, the internal sensing method where particular analytes are injected into the internal channel. However, the internal analyte channel is difficult to fabricate due to the internal metal-coating process. Moreover, it is challenging and sensitive due to analyte injection into and ejection from the internal channels. The second category SPR sensor based on analyte position is the external sensing method where the analyte channel is placed in the exterior of the sensor structure. The external sensing approach provides benefits such as easy manufacturing and efficient controlling of the analytes' inflow and outflow. Based on the shape, the SPR sensor can be categorized as; circular-shaped, D-shaped top polished, D-shaped top polished with microchannel, D-shaped with both sides polished with microchannel, etc. All of these sensors are designed to detect the unknown RI of a single analyte. If the sensor is capable of detecting multi-analyte, then it is termed as a multi-analyte sensor. Generally, more than one channel is used to detect multi-analyte. Multi-channel with multi-analyte sensors offer several advantages such as the ability to detect multiple samples on the same structure, save time by quick detection ability, reduce cost by housing multiple sensors on the same platform.

Being motivated by the concept, we propose a multi-channel with multi-analyte PCF-SPR sensor, which is expected to sense multiple analyte simultaneously.

1.2 Objectives

The overall objective of this thesis is to design a three-channel PCF-SPR sensor with a minimum number of circular air holes while simultaneously achieving much higher sensitivity, resolution, figure of merit, etc. than the existing designs in the literature. This objective will be achieved through the following specific aims:

- To perform an in-depth literature review of PCF-SPR sensors with a focus to multi-channels and multianalytes.
- To explore Gold (Au) along with Tantalum Pentoxide and Titanium Dioxide as plasmonic materials to be used with the PCF structure.
- To design and simulate multi-channel and multi-analyte PCF sensor structures with circular-only air holes keeping their number minimum, using full-FEM.
- To study the modal characteristics and to increase the detection range of sample analytes by optimizing the geometric parameters of the multi-channel sensor with enhanced sensitivity, resolution, and linearity.
- To validate its superiority, the performance parameters of the multi-channel and multi-analyte sensor will be compared with those of the recent literature.

1.3 Possible Outcome

The possible outcome is a successful design of a simple yet highly sensitive multi-channel and multi-analyte sensor with superior performance outperforming all multi-channel and multi-analyte sensors to date. Hence, it is anticipated that the proposed sensor will have a high impact in detecting unknown RI for chemical, biochemical, and biomedical applications.

1.4 Methodology

To design PCF based SPR sensor following steps will be followed:

First, the PCF structure will be designed with commercially available COMSOL Multiphysics 5.5 software. FEM will be utilized to solve the Maxwell equation to understand and study various complex modal characteristics of the sensor. To achieve perfection in simulation and achieve accurate results, sensor structure will be meshed with extremely fine element size. Furthermore, a cylindrical, perfectly matched layer (PML) with scattering boundary conditions will be employed beyond the outer boundary to obtain accurate modal solutions. The plasmonic materials will be employed in channels. For example, in channel-1, Au will be used as plasmonic materials. Whereas Au with Tantalum Pentoxide and Au with Titanium Dioxide will be utilized in channel-2 and channel-3 respectively. RI of silica will be obtained by Sellmeier equation. RI of Au, Tantalum Pentoxide and Titanium Dioxide will be obtained by Drude-Lorentz model.

Second, Mode analysis for different analyte RI at different wavelengths (visible to IR) ranges will be studied as per channel to look for resonant wavelength and CL peaks.

Third, a numerical investigation will be carried out with the help of obtained resonant wavelength and CL peaks. The analysis includes wavelength interrogation, amplitude interrogation, finding resolution, determining the FOM, etc.

Fourth, the results of the investigation will be compared with the recently reported similar types of research works to measure the weight of this thesis. In the process of investigation, different numerical tools will be used in this thesis. COMSOL Multiphysics will be used for designing, meshing, modal analysis, and result analysis. Microsoft Excel, Origin, CurveExpert, etc will be used to assess the performance of the multi-analyte and multi-channel sensor, CL, and sensitivity curve and to preserve the data collected from COMSOL software and plotting these data to measure various parameters.

1.5 Thesis Outline

Chapter 2 will focus the literature study. Basic knowledge related to photonic PCF and SPR will be discussed. Furthermore, the sensing principle with photonic crystal fiber and the application of photonic crystal fiber sensors will be highlighted. At the end of the chapter literature review will be presented.

Chapter 3 will highlight the sensor related theory and step by step sensor design topology. At the end of the chapter, the simulation setup will be discussed.

The basic structure of the proposed multi-channel and multi-analyte sensor will be optimized in **chapter 4**. At the beginning of the basic structure optimization, a set of initial structural parameters will be utilized by previous knowledge and with an intelligent guess. Parameters like pitch, thickness, air-hole diameters and distance between air-holes will be optimized.

Chapter 5 will describe the step-by-step optimization of three different channels of the proposed sensor. At the beginning of multi-channel optimization, the gap between three different channel will also be optimized. In the process of optimization, the confined structural values from the previous chapter will be utilized. As the plasmonic material is different for the three channels, therefore, separate optimization will be carried out as per channels.

Based on the optimized parameters from last chapters, **chapter 6** will highlight the obtained results and discuss the results with the help of different measuring parameters. For example, WS, AS, sensor's resolution, merit figure, etc. At the end of the chapter, the achieved results will be compared with the previous research works to judge the merit of the proposed work.

Chapter 7 will highlight the possible application of the proposed multi-channel and multi-analyte sensor. The RI of many analyte samples may fall within the achieved RI range of the proposed sensor. However, in this thesis, we shall highlight the detection of cancerous cells with different channels of the proposed sensors.

In **Chapter 8**, we shall discuss the fabrication feasibility of the proposed sensor. Before discussing the possible fabrication techniques, we shall test the fabrication tolerance of the proposed model by varying different structural parameters.

Chapter 9 is the conclusion section, where we shall formally terminate the thesis with concluding remarks. Furthermore, the direction of the future research will be highlighted at the end.

Chapter 2

Literature study

2.1 Photonic Crystal Fiber and Surface Plasmon Resonance

2.1.1 Photonic Crystal Fiber

PCF, a novel type of optical fiber based on photonic crystal characteristics, has revolutionized the field of fiber optics by allowing for a new manner of steering light that is not achievable with traditional optical fibers. A photonic crystal is a microstructured material made up of low- and high-index materials that have been periodically shaped in one, two, or three dimensions with a characteristic length or period on the order of the wavelength. The uniform arrangement of fused silica and air holes or spaces in a simple PCF microstructures it transversely at a size comparable to the wavelength of the electromagnetic radiation directed by the fibre[10]. **Fig 2.1** shows PCF with different lattice configuration.

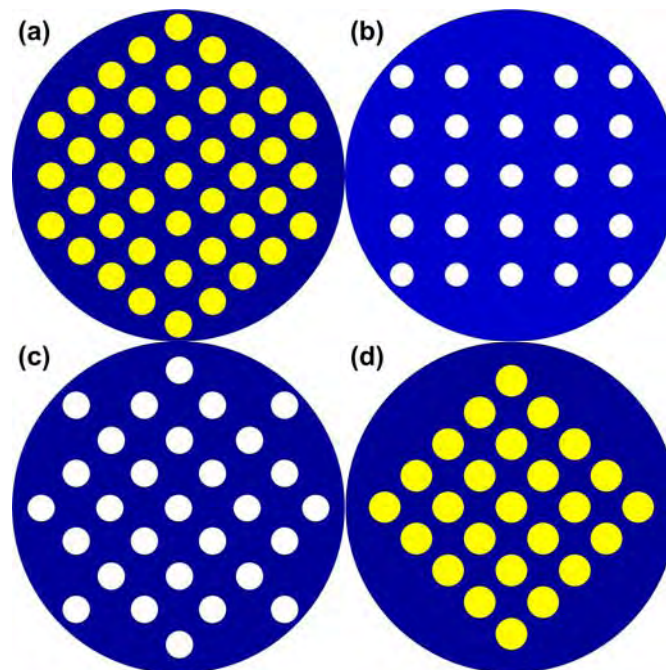


Fig. 2.1 (a) to (d) Schematic Diagram of PCF with different lattice configuration

2.1.1.1 History of PCF

The first concept of PCF was developed by Yeh et al. in the year 1978[11]. He proposed cladding a fiber core with Bragg grating. This is similar to a one-dimensional photonic crystal. In 1992, P. Russell developed a PCF having a 2D photonic crystal with an air core. The first PCF was realized in 1996 by P. Russel. Since Russell's discovery, there has been a surge in research interest in this form of the waveguide in the realm of optical fiber technology. J. C. Knight, on the other hand, has created a new dimension in the realm of nonlinear optics by fabricating the first PCF for regulating light in the fiber [13].

2.1.1.2 Light Guiding Mechanism Through Fiber

The index of refraction in fiber is a measure of the speed of light in the material. This index changes according to the property of the material. Beyond a certain angle, the refraction will cause light to be reflected from the surface. Optical fiber uses this reflection property to confine light in the fiber's core by choosing core and cladding materials with the proper index of refraction that will cause all the light to be reflected if the angle of the light is below a certain angle. That angle is referred to the total internal reflection(TIR). Beyond a certain angle, the refraction will cause light to be reflected from the surface. The light-guiding basic principle on which traditional optical fiber works is the TIR. Fig 2.2 shows the light propagation mechanism in the fiber.

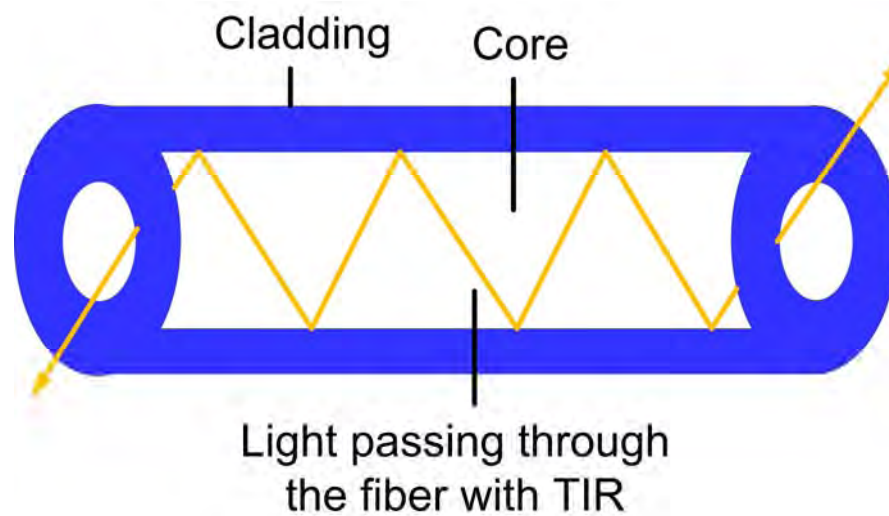


Fig. 2.2 TIR principle in guiding light through fiber.

2.1.1.3 Light Guiding Mechanism through PCF

In the case of PCF, the fiber contains a massive core surrounded by an array of air-holes running all along the fiber length. By selecting a core material with a higher refractive index than the cladding effective index, a two-dimensional photonic crystal can be used as a fiber cladding. A PCF with a silica solid-core surrounded by a photonic crystal cladding with a triangular lattice of air-holes, hollow-core PCF and their light guiding mechanism is shown in **Fig. 2.3**. These fibers, also known as index-guiding PCFs, guide light by modified TIR, a total internal reflection type. They do, however, differ from traditional optical fibers in several ways[16, 17].

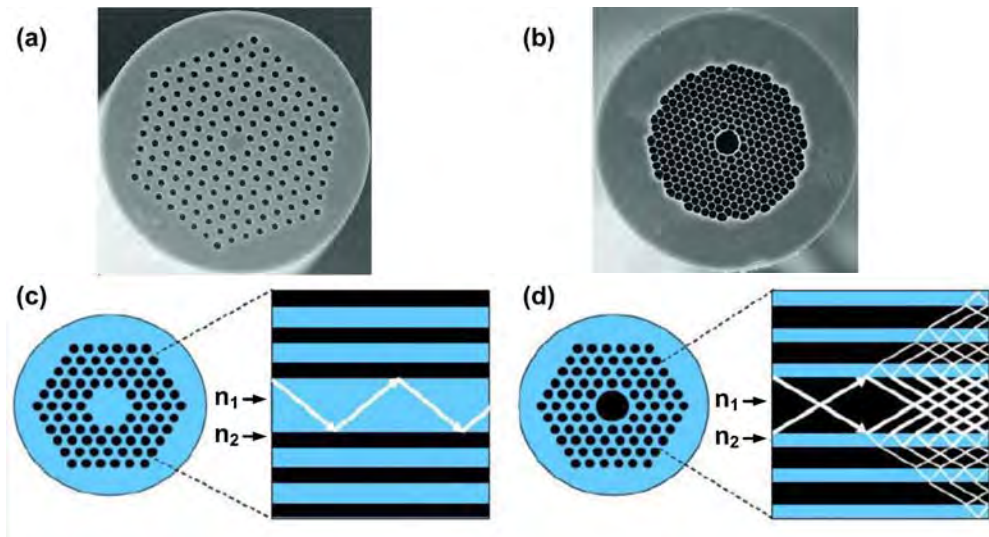


Fig 2.3. (a) Microscopic image of solid-core PCF (b) Microscopic image of hollow-core PCF (c) Light guiding mechanism in solid-core PCF with modified TIR (d) Light guiding mechanism in hollow-core PCF with bandgap effect[16-17].

2.1.2 Surface Plasmon Resonance

2.1.2.1 SPR Basis

SP are the confined waves at the boundaries between a thin metal and a dielectric that occur due to coupling electron-photon modes [18, 19]. SPR is a simple, direct, and label-free optical technique for measuring refractive index changes in the vicinity of a thin metal layer whose conduction band electrons can be modeled as free-electron plasma. When light with the same wave vector as a SP is incident on a metal surface, this phenomenon occurs. This causes a charge density wave to propagate along with the

metal-dielectric contact due to the collective oscillation of free electrons on the metal surface. SPs are collective oscillations that are sensitive to changes in the dielectric constant of the medium near the metal surface[20].

In both plasmonic metal and dielectrics, SPs are accompanied by a longitudinal (TM or p-polarized) electric field that degenerates exponentially. The field has its peak at the metal-dielectric interface for this exponential decay of electric field intensity. Solving Maxwell's equation for metal-dielectric kind of RI distribution yields both of these important characteristics of SPs being TM-polarized and exponential decrease of electric field. One can also prove that the SP wave propagation constant (K_{SP}) over the metal-dielectric interface is determined by solving Maxwell's equation[21].

$$K_{SP} = \frac{\omega}{c} \left(\frac{\epsilon_m \epsilon_s}{\epsilon_m + \epsilon_s} \right)^{\frac{1}{2}} \quad (1)$$

The dielectric constants of the metal layer and the surrounding dielectric medium are denoted by ϵ_m and ϵ_s , respectively. The velocity of light is indicated by c , and the frequency of incident light is denoted by ω . The relationship above shows that the properties of the SP wave vector are affected by both media[21]. Now to generate SP oscillations in the metal (conductor) electrons need to be excited. So imposing the light (electromagnetic field) on the surface is necessary. The highest propagation constant of the light wave at frequency traveling through the dielectric medium is given by[21]:

$$K_s = \frac{\omega}{c} \sqrt{\epsilon_s} \quad (2)$$

We know that electrical permittivity for metal is negative and electrical permittivity for dielectric is positive; therefore, the propagation constant of the light wave is less than the propagation constant of SP. As a result, direct light cannot trigger SPs at the metal-dielectric interface, which is referred to as nonradiative SP. As a result, the momentum and wave vector of the exciting light in the dielectric medium should be enhanced to excite SPs[21].

2.1.2.2 Excitation of SPR

2.1.2.2.1 Otto Configuration

The tail of the evanescent wave at the glass-air interface is brought into touch with a metal-air interface in the Otto design, which supports SPW. The presence of the metal has only a little effect on the evanescent wave when the gap width is large enough. A surface plasmon resonance condition is achieved by selecting an appropriate angle of incidence of the completely reflected beam within the prism. Due to radiation damping of the SPW, the resonance is stretched and shifted for a short gap - width, whereas a large gap - width leads to ineffective excitation of the SPW or no SPR condition[22]. A graphical representation of Otto configuration is shown in **Fig. 2.4 (a)** [23].

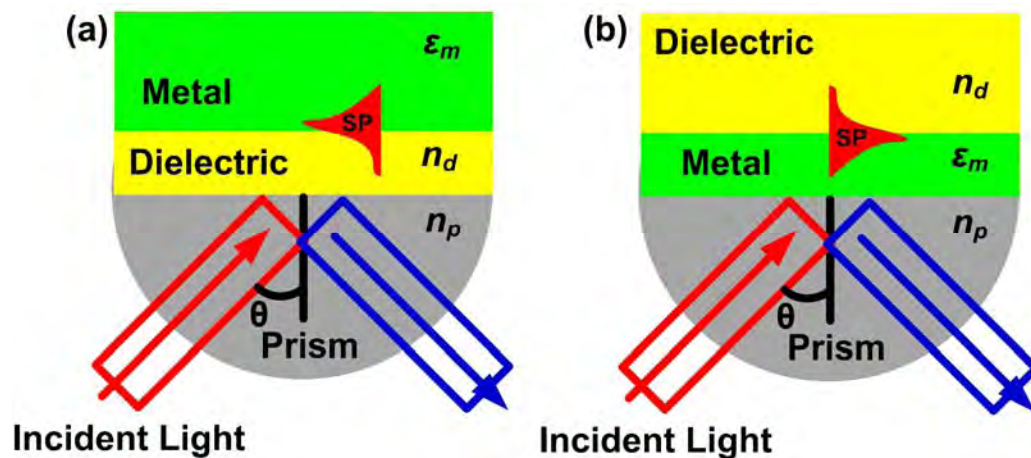


Fig. 2.4. Surface plasmon polariton (SPP) excitation method (a) Otto configuration. (b) Kretschmann configuration

2.1.2.2.2 Kretschmann Configuration

The Kretschmann method is the most prevalent configuration in which a thin metal sheet is evaporated on top of a glass prism. The surface plasmon resonance condition is achieved by adjusting the angle of incidence of the completely reflected beam inside the prism to a suitable value. The evanescent wave formed at the metal-glass interface must penetrate the metal layer in order to activate a surface plasmon at the metal-air interface in the Kretschmann arrangement. Because of radiation damping into the glass, if the metal is too thin, the SPW will be substantially damped. However, if the metal is too thick, the SPW can no longer be efficiently stimulated due to metal absorption. As a result, the thickness of the metal has a significant impact on SPW excitement[22]. A graphical representation of Kretschmann configuration is shown in **Fig. 2.4 (b)** [23].

2.1.2.3 Sensing Principle

When the real part of effective RI (n_{eff}) of core-guided mode and surface plasmon polaritons (SPP) mode values coincide in SPR, resonance occurs. Maximum energy transfers from the core-guided mode to the SPP mode at resonance. Because the RI of the dielectric medium (sample) changes, the n_{eff} of SPP changes, resulting in a lower resonance peak and a shift in resonance wavelength. This means that depending on the RI of the sample/analyte, the phase-matching wavelength changes. The variation of peak loss due to the change of analyte's RI can be used to identify an unknown sample concentration. The major parameter for measuring the sensing performance of the PCF SPR sensors is the wavelength and amplitude interrogation methods. In the exterior of PCF structure (cladding) appropriate metal (with plasmonic property), coating will improve the interaction of the evanescent field with surface free electrons, which will boost the sensor's sensitivity. The easy interaction with the metal layer's free electrons results in a high coupling between the core guided and SPP modes, which improves sensor performance[24].

2.1.2.4 Photonic Crystal Fiber Based SPR Sensor

Light propagation in PCF can be controlled as there are air-holes in the cladding region. PCF follows attenuated TIR for the propagation of light. Light propagation can be tuned in PCF by arranging different sizes of air-hole and by introducing number rings of air-holes. PCF-SPR sensors offer several advantages such as compactness, robustness, low cost, label-free sensing, the capability of remote sensing, miniaturization, real-time sensing capability, and flexible design[25].

2.1.2.5 Application of SPR based sensor

Currently, the best-known application area of SPR sensors is related to biochemical research, such as, in the identification of antigen–antibody interactions, enzymatic reactions, drug screening and forensics, the search for new bio-markers, and proteomics [26]. Other applications include genomics, medical diagnostics, environmental monitoring, food analysis, and security [27, 28].

2.2 Literature Review

Recently, some researchers have reported multi-channel and multi-analyte sensors, for example, P. Bing et al. proposed a two-channel PCF-SPR sensor in the RI range of 1.33-1.40 with a wavelength range of 595-918 nm using Au (channel A) and Au with a dielectric (channel B)[1]. The reported sensor achieved WS of 11600 nm/RIU and 10600 nm/RIU, for the two channels, respectively. However, it is challenging to practically realize the sensor due to very high CL (near to 5800 dB/cm). Because the length of the sensor is inversely proportional to the CL. Furthermore, other associated loss for example bending loss, splicing loss, input-output loss along with high CL may give misleading spectra. M. F. O. Hameed et al.[6] designed a two channel sensor with narrow RI range (1.33-1.35) and moderate sensitivity (4750 and 4300 nm/RIU). However, it has high CL (300 dB/cm) and complex design due to the presence of three types of air-holes. In 2020, A. Yasli et al. [3] reported a two channel sensor with narrow RI range (1.33-1.36) and low sensitivity (2500 and 3083 nm/RIU). Furthermore, the design of this sensor is complex due to the presence of the four types of air-holes. V. Kaur et al. designed a two-channel PCF-SPR sensor based on Au with an internal analyte channel in the wavelength range of 813-1100 nm range in the RI range from 1.30-1.40[5]. The reported sensor achieved 1000 nm/RIU and 3750 nm/RIU WS in channel-1 and channel-2, respectively, whereas, in the case of AS, channel-1 and channel-2 achieved only 0.5 RIU^{-1} and 40 RIU^{-1} , respectively. Again, this sensor has CL as high as 5449 nm/RIU, making it challenging to realize practically. Furthermore, internal sensing, on the other hand, has several disadvantages, including fabrication difficulty due to internal metal coating, slow operation, and time-consuming analyte handling in the analyte channel[29]. Again in 2020, A. Yasli et al. proposed a two-channel sensor with narrow RI range (1.34-1.37) and lower sensitivity (4100 and 3700 nm/RIU). This sensor has high confinement loss (500 dB/cm) [9]. R. Otupiri et al. reported a four channel sensor employing Au and Ta_2O_5 with narrow RI range (1.33-1.35) and low sensitivity (4600 and 2300 nm/RIU). This sensor also has high CL (480 dB/cm) [4]. S. I. Azzam et al. designed a four channel sensor. The achieved RI range of this sensor is only 1.33-1.34 and it has very high CL (1400 dB/cm) [8]. Firoz Haider et al. reported an Au-coated grapefruit PCF sensor with three channels. Channel-1 was working in the 1.33-1.35 RI range with WS of 2000 nm/RIU, channel-2 working in the 1.36-1.38 RI range with WS of 3000 nm/RIU, and channel-3 exhibiting higher performance, in the 1.39-1.42 RI range with a maximum WS of 18000 nm/RIU[7].

As can be seen, all three channels do not perform equally well. Moreover, internal coating and sensing pose additional challenges, as mentioned above. All these reported multi-channel and multi-analyte sensors have significantly higher CL, hence, the usable fiber length will not be practical. Furthermore, these sensors suffer from lower sensitivity and non-uniform performance among the channels. Additionally, the achieved RI range of the reviewed literature is quite narrow. Thus, multi-channel with multi-analyte sensors require further research to achieve practically realizable CL, wider RI range, higher sensitivity (both wavelength and amplitude), a higher FOM, and similar better performance in all the channels.

2.3 Summary

This chapter discusses the basic knowledge regarding the PCF and SPR. At the end of the chapter, the literature review related to multi-channel and multi-analyte sensing is presented to identify the research gap. In the next chapter, sensor-related theory and step-by-step optimization will be carried out.

Chapter 3

Sensor Related Theory and Step by Step Design

3.1 Sensor Related Theory

The basic structure of the PCF-SPR based sensor is the silica. The RI of silica varies with the wavelength of incident light. For simulation purpose the wavelength dependent Sellmier equation will be used to calculate its RI. Sellmier equation was utilized to obtain the RI of fused silica[30]:

$$n_1(\lambda) = \sqrt{1 + \frac{a_1\lambda^2}{\lambda^2 - b_1^2} + \frac{a_2\lambda^2}{\lambda^2 - b_2^2} + \frac{a_3\lambda^2}{\lambda^2 - b_3^2}} \quad (3)$$

where \mathbf{a} and \mathbf{b} are the Sellmier coefficients for silica glass as given below:

$$\begin{aligned} a_1 &= 0.6961663, a_2 = 0.4079426, a_3 = 0.8974794 \\ b_1 &= 0.0684043 \mu\text{m}, b_2 = 0.1162414 \mu\text{m}, b_3 = 9.896161 \mu\text{m} \end{aligned}$$

The main plasmonic material of the proposed sensor is Au. However, the thickness of Au varies in different channels. Au layer thickness, t_{Au} in channel-1, channel-2, and channel-3, respectively as the primary plasmonic material which is subject to the step-by-step optimization. Several methods such as sputtering, thermal evaporation, electron-beam technique, etc. can be used to deposit Au on the exterior surface of the sensor. The permittivity of Au is given by the following expression[31]:

$$\varepsilon_{\text{Au}} = \varepsilon_{\infty} - \frac{\omega_D^2}{\omega(\omega + j\gamma_D)} - \frac{\Delta\varepsilon \Omega_L^2}{(\omega^2 - \Omega_L^2) + j\Gamma_L\omega} \quad (4)$$

where, ε_{Au} = permittivity of gold, $\varepsilon_{\infty} = 5.9673$ = permittivity at high frequency. The angular frequency = $\omega = 2\pi v/\lambda$, where v is the velocity of light. ω_D and γ_D are the plasma frequency and damping frequency, respectively, whereas $\omega_D/2\pi = 2113.6$ THz and $\gamma_D/2\pi = 15.92$ THz. The weighting factor = $\Delta\varepsilon = 1.09$. While $\Omega_L/2\pi = 650.07$ THz and $\Gamma_L/2\pi = 104.86$ THz are the oscillator strength and spectral width of the Lorentz oscillators, respectively.

Ta₂O₅ is a transparent metal oxide with a high fusion point, wider spectrum range, low loss (waveguide loss ~ 1 dB/cm), high melting point. A thin layer of Ta₂O₅ along with Au will be used in channel-2 along with Au layer. Due to Ta₂O₅ overlayer, additional field energy is required to excite a strong enough plasmon for sensing which ultimately shifts the resonance wavelength than using only Au in the channel. Thus using Ta₂O₅ overlayer in the channel-2 makes a difference with channel-1 in terms of resonance wavelength. Consequently, using Ta₂O₅ in the channel-2 will make simultaneous detection possible. Appropriate thickness layer of Ta₂O₅ was deposited over the Au layer in channel-2 which will be confirmed by step-by-step optimization. RI of Ta₂O₅ is calculated from[32]:

$$n_{Ta_2O_5} = 1.878 + \frac{178.4 \times 10^2}{\lambda^2} + \frac{52.7 \times 10^7}{\lambda^4} \quad (5)$$

where n is the RI of Ta₂O₅ and λ represents the wavelength in nm.

TiO₂, a photocatalytic material, exhibits lossy mode resonance under certain conditions[33]. TiO₂ is a transparent and has a higher RI which can be used as a transition metal. As a result, a huge number of electrons can be created at the metal–dielectric interface's surface[34, 35]. TiO₂ layer provides protection and adhesion to the Au layer and prevents flake off [36]. Appropriate TiO₂ layer coating on the PCF-SPR sensor enhances RI sensitivity and redshifts the resonant wavelength towards the telecommunication wavelength region[37]. Using TiO₂ along with Au layer in the channel will result different resonant wavelength than using only Au. Achieving different resonant wavelength among the channel for the same RI is important because, it would allow the channel to sense analyte simultaneously. A detail study of TiO₂ layer thickness on the performance of the sensor will be discussed in the subsequent chapter. Appropriate

thickness layer of TiO₂ will deposited over the Au layer in channel-3 which will be confirmed after step-by-step optimization. Wavelength dependent RI of TiO₂ was calculated with the following formula[34]:

$$n^2 = 5.913 + \frac{2.441 \times 10^7}{(\lambda^2 - 0.803 \times 10^7)} \quad (6)$$

where n is the refractive index of TiO₂ and λ represents the wavelength in μm .

The evaluation of a PCF-SPR sensor is based on CL. To calculate the CL of the sensor, the imaginary part of the RI (n_{eff}) is used. CL describes the SPR sensor's performance [30, 31]. CL of the sensor can be calculated as[38]:

$$\alpha_{LOSS} = 8.686 \times \frac{2\pi}{\lambda} \text{Im}(n_{eff}) \times 10^4 (\text{dB/cm}) \quad (7)$$

where λ is the operating wavelength in μm and $\text{Im}(n_{eff})$ represents the imaginary part of the effective RI.

When the RI of analyte or sample changes then the resonant wavelength of the sensor changes. Utilizing this change, the sensitivity of the sensor can be measured. The change in resonance wavelength in nm with respect to the change in RIU of the target analyte is defined as WS[5]. Sensor's WS is calculated as[39]:

$$S_\lambda = \frac{\Delta\lambda_{peak}}{\Delta n_a} \quad (8)$$

where S_λ denotes the WS and expressed in nm/RIU, $\Delta\lambda_{peak}$ is the wavelength peak shift in nm for any n_a variation and Δn_a is the variation between two adjacent n_a .

The sensor's resolution is its capability to observe the slightest difference in the target analyte[40]. The sensor' resolution can be calculated with the help of wavelength interrogation method. The wavelength resolution of the sensor is given by the following equation[41]:

$$R(RIU) = \Delta n_a \times \frac{\Delta\lambda_{min}}{\Delta\lambda_{peak}} \quad (9)$$

where $\Delta n_a = 0.01$ (considered in this work) is the variation between two neighboring n_a , $\Delta \lambda_{min}$ is the minimum spectral resolution which was considered as 0.1 nm and $\Delta \lambda_{peak}$ denotes the shift in resonant wavelength peak.

AS is an interrogation method that is executed at a single operating wavelength. Spectral manipulation is not required in AS investigation and thus its operation is simple and offers lower cost[42]. The AS of the sensor can be measured by the following equation[43]:

$$s_A(\lambda)(RIU^{-1}) = -\frac{1}{\alpha(\lambda, n_a)} \times \frac{\partial \alpha(\lambda, n_a)}{\partial n_a} \quad (10)$$

where $\alpha(\lambda, n_a)$ is the CL value for any n_a at specified λ , $\partial \alpha(\lambda, n_a)$ is the CL difference for a specified λ between two adjacent analyte RIs and ∂n_a is the difference between two adjacent analytes RI.

FOM is one of the sensing performance indicators where higher FOM means greater detection accuracy[44]. The performance of the proposed sensor was evaluated in terms of FOM for the three channels. FOM can be measured by the following equation[45]:

$$FOM = \frac{S_\lambda}{FWHM} \quad (11)$$

where S_λ is the WS calculated in nm/RIU and FOM is measured in RIU^{-1} . Length of FWHM is calculated from the CL curve. FWHM is de-abbreviated as the full width at half maximum which is calculated in nm.

3.2 Step by Step Design Topology

Most of the multi-channel sensors have either two channels or four channels. However, this research work aimed at designing a tri-channel sensor. Therefore, to keep the structure simple, three analyte channels with uniform channel depth were planned. Also, the design ensures that all three channels get equal light-matter interaction. Thus air holes are arranged in such a way that incident light can reach towards three channels equally.

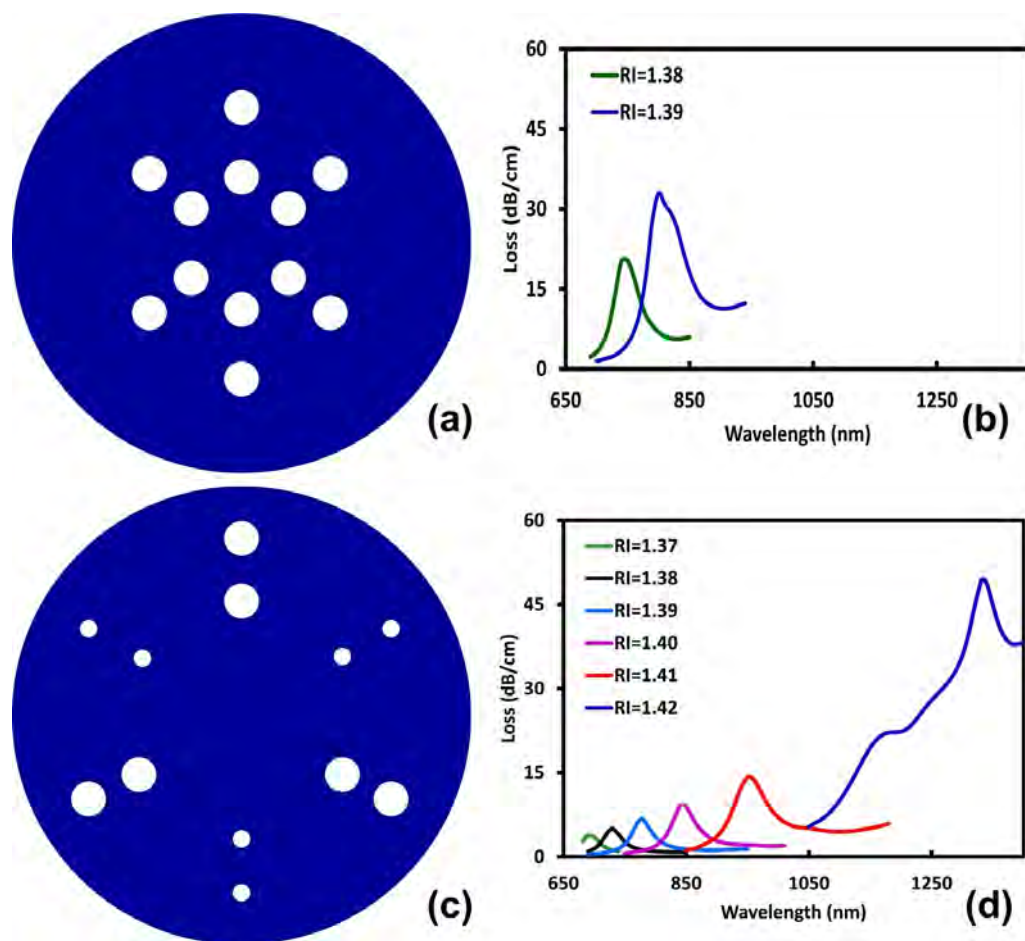


Fig. 3.1. Step-by-step design procedure of the proposed sensor. (a) Truncating a regular PCF with core (b) Corresponding loss spectra of the sensor with the structure shown in (a). (c) and (d) Modified structure and Corresponding CL spectra as per new design

Fig. 3.1 shows the step-by-step design procedure of the structure for the proposed multi-channel PCF-SPR sensor. Firstly, keeping in mind that sufficient interaction should take place between the core-guided mode and the SPP mode, a segment of the PCF, including the hexagonal core was cut (see **Fig. 3.1(a)**) to form the initial structure). The primary structure exhibits SP resonance with a wavelength range from 750 nm to 800 nm for the analyte RI range 1.38-1.39 only (see **Fig. 3.1(b)**). Because of the shorter RI range and limited operating wavelength region, this structure is not acceptable.

The leakage of the the core guided mode needs to be made more lossy to find SP resonance for a broad RI range in a wider operating wavelength region. To do this, the core size was made bigger by shifting core air-holes outward. Similarly, to reduce index contrast in the cladding region the cladding air-hole is also shifted towards the cladding region. Furthermore, to ensure more interaction between the core-guided mode and plasmonic mode, the size of air-holes in between the channels were made half the initial structure. The outcome of this modification is the structure in **Fig. 3.1(c)** (bottom left). As can be seen from Fig 3.1 (d) that the SP resonance takes place for a more comprehensive RI range of 1.37–1.42. Furthermore, the operating wavelength (690-1170 nm) has increased significantly. Hence, the structure as shown in **Fig. 3.1(c)**, (bottom row) is considered as the reference structure whose structural parameters will now be tuned over a range to achieve optimum sensor performance.

Fig. 3.2 depicts a cross-sectional schematic of the proposed PCF-SPR sensor (reference structure), along with the geometric parameters that are to be optimized. It consists of twelve circular air-holes in two layers. The inner layer constitutes the core, and the outer layer the cladding. Air-holes are of two sizes with a diameter $d_1 = 1 \mu\text{m}$ and $d_2 = 0.5 \mu\text{m}$ respectively.

Larger air-holes in a pair are placed 120° apart to make three distinct channels. The beginning and end of a pair of larger air-holes demarcate one channel. The right channel (from the center) is marked a channel-1, and it is consecutively marked as channel-2 and channel-3 counter-clockwise. Inter channel gap for this multi-channel sensor is considered as $d_g = 1 \mu\text{m}$. In between two pairs of larger air-holes a pair of smaller air-holes are placed just to help the evanescent field couple with the plasmonic mode for stronger light-matter interaction. Distance between two air-holes in any pair is considered as $d_3 = 1.5 \mu\text{m}$. The Pitch, $\Lambda = 2 \mu\text{m}$ is employed for the structure. Center of inner air-holes are spaced apart from center of the core with a distance $d_4 = 3.5 \mu\text{m}$. As shown in the following section, the optimal values of geometric parameters such as d_1 , d_2 , d_3 , d_4 , d_g , and Λ are obtained after an extensive investigation by varying them over a range and evaluating their effect on the sensor performance. **Fig. 3.3** shows the electromagnetic field distribution of SPP modes and fundamental core modes for channel-1, channel-2, and channel-3, respectively. The color bar at the right of Fig. 3 indicates the field intensity distribution of normalized mode.

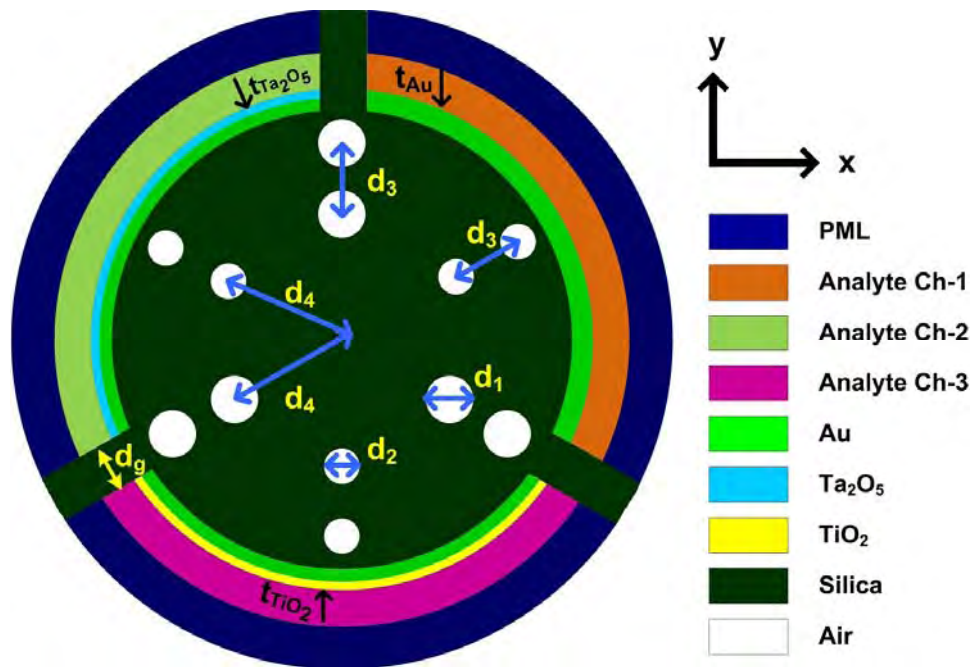


Fig. 3.2. The proposed multi-channel Sensor's cross-section schematic, demonstrating several geometric parameters.

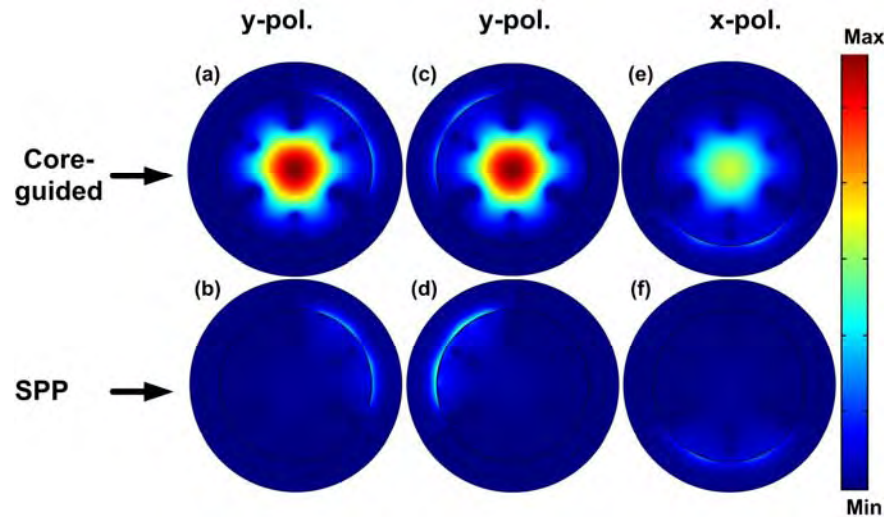


Fig. 3.3 Electromagnetic field distribution. (a-b) y-polarized core guided and SPP modes for $n_a = 1.41$ in channel-1 (c-d) y-polarized core guided and SPP modes for $n_a = 1.41$ in channel-2 (e-f) x-polarized core guided and SPP modes for $n_a = 1.41$ in channel-3.

3.3 Simulation Setup

To study the complex modal properties of the analyzed structures, the Web Optics module of commercially available FEM-based software COMSOL Multiphysics was used. Furthermore, in COMSOL, the sensor's structure was meshed with extremely fine element size under 'physics-controlled mesh' scheme to get accurate results. With 423049 numbers of degree of freedom the sensor structure was solved. The features of mesh statistics are as follows, the number of vertices = 61409, number of elements = 122062, minimum element quality = 0.3945, Average element quality = 0.8705, and mesh area = $194.1 \mu\text{m}^2$. Also, a cylindrical anisotropic perfectly matched layer (PML) of $1 \mu\text{m}$ thickness with scattering boundary conditions was employed beyond the outer boundary to obtain accurate modal solutions.

3.4 Summary

This chapter described the sensor's related theory. Various measuring parameters for the evaluation of sensor's performance with formula has been explained. Then, step by step design topology of the proposed sensor has been elaborated. At the end of the chapter, the simulation setup for the proposed PFC-SPR multi-channel with multi-analyte sensing has been narrated. In the coming chapter, sensor's basic structure optimization will be described.

Chapter 4

Sensor's Basic Structure Optimization

4.1 Pitch optimization

At the beginning of reference structure optimization, an initial value of structural parameters such as Au layer thickness, $t_{Au} = 50$ nm, the diameter of larger air-hole, $d_1 = 1.0$ μm , the diameter of smaller air-hole, $d_2 = 0.5$ μm , and distance between adjacent air-holes, $d_3 = 1.5$ μm were set. To find the optimal value, the pitch, $\Lambda = 2.2, 2.0,$ and 1.8 μm was varied. Fig. 4.1 shows the CL plots of varying pitch. For pitch, $\Lambda = 2.2$ μm the sensor achieves a maximum WS of 22000 nm/RIU with a RI range of 1.39-1.42. In the case of, pitch, $\Lambda = 2.0$ μm the sensor achieves a maximum WS of 23000 nm/RIU for an RI detection range of 1.37-1.42. Finally, for pitch, $\Lambda = 1.8$ μm the sensor achieves the maximum WS of 20000 nm/RIU with an RI range of 1.37-1.42. Considering the more comprehensive RI range and higher WS, pitch, $\Lambda = 2.0$ μm was considered optimal for the proposed sensor. Note that, the distance of nearest air-holes from the center, d_4 is related to the pitch (Λ). Thus, with the optimization of pitch (Λ) the distance d_4 has automatically been optimized.

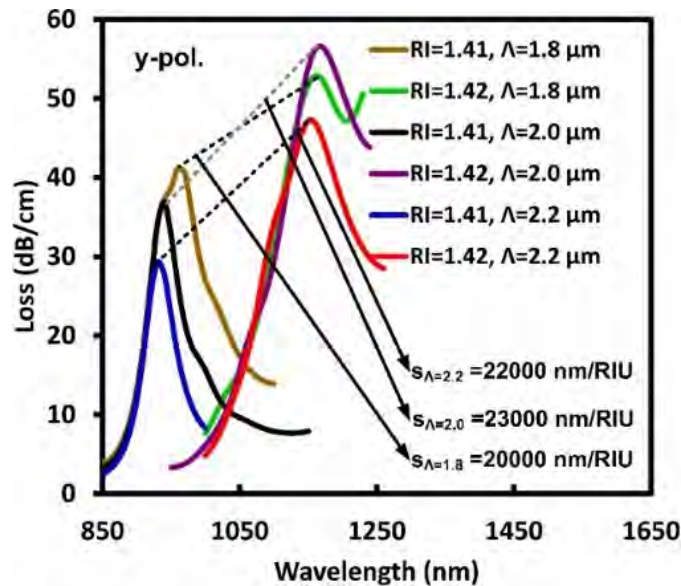


Fig. 4.1 Pitch variation effect on the basic structure. CL spectra for pitch, $\Lambda = 1.8, 2.0,$ and 2.2 μm for RI of 1.41-1.42.

4.2 Optimization of Air-holes (d_1 and d_2)

In the proposed sensor, there are two types of air-holes such as larger air-hole with a diameter d_1 and smaller air-hole with a diameter d_2 . Total eight combinations of diameters of the two sizes of air-holes were varied to find the best pair. During the optimization process, the pitch $\Lambda = 2 \mu\text{m}$, and Au layer thickness, $t_{\text{Au}} = 50 \text{ nm}$ were kept as fixed. As a general pattern, it can be seen that increasing the diameter of larger air-hole reduces CL, and decreasing the diameter of smaller air-hole increases CL. The reason is, reduced smaller air-holes allures more light towards the plasmonic layers for increased light-mater interaction. Different measuring parameters that were obtained during the air-hole diameter optimization investigation are tabulated in **Table 4.1**. As can be seen from the table that for $d_1 = 1.0 \mu\text{m}$, $d_2 = 0.4 \mu\text{m}$ and for $d_1 = 1.0 \mu\text{m}$, $d_2 = 0.5 \mu\text{m}$ performances are very close considering RI range, WS, AS, and FOM. However, based on the criteria of higher average FOM and lower maximum CL $d_1 = 1.0 \mu\text{m}$, $d_2 = 0.5 \mu\text{m}$ are considered as optimal air-hole diameters for larger and smaller air-holes, respectively.

TABLE 4.1 AIR-HOLES DIAMETER (D_1 AND D_2) VARIATION EFFECT

d_1 (μm)	d_2 (μm)	Max. WS (nm/RIU)	Max. FOM (RIU ⁻¹)	Avg. FOM (RIU ⁻¹)	RI Range (RIU)	Max. CL (dB/cm)
0.8	0.5	23000	460.00	277.50	1.38-1.42	67.422
0.8	0.4	23000	460.00	277.50	1.38-1.42	77.899
1.0	0.4	23000	383.33	228.88	1.37-1.42	66.129
1.0	0.5	23000	383.33	236.66	1.37-1.42	56.53
1.0	0.6	22000	314.28	215.19	1.37-1.42	48.978
1.2	0.4	23000	342.85	215.90	1.37-1.42	57.587
1.2	0.5	23000	287.50	198.76	1.37-1.42	48.353
1.2	0.6	22000	275.00	229.16	1.38-1.42	41.249

4.3 Au Thickness layer (t_{Au}) optimization

The performance of the PCF-SPR sensor depends significantly on the thickness of the plasmonic layer. The thickness of the Au layer of the reference structure needs to be optimized because it would serve as the initial thickness layer in the three channels of the proposed multi-channel and multi-analyte sensor. Au layer thickness, $t_{Au} = 45, 50, 55,$ and 60 nm were varied to find optimal thickness. **Fig. 4.2** shows the plot of WS as a function of wavelength for thickness variation. For Au layer thickness, $t_{Au} = 45, 50,$ and 55 nm, the reference structure showed a similar response in maximum WS (23000 nm/RIU). However, with Au layer thickness, $t_{Au} = 45$ nm, the detectable RI range is $1.38-1.42$, and thus it is discarded. Because for Au layer thickness, $t_{Au} = 50$ and 55 nm, the detectable RI range is $1.37-1.42$. However, with Au layer thickness, $t_{Au} = 50$ nm, the maximum FOM (383.33 RIU $^{-1}$) and average FOM (236.66 RIU $^{-1}$) are higher than the maximum FOM (255.55 RIU $^{-1}$) and average FOM (196.11 RIU $^{-1}$), which results with $t_{Au} = 55$ nm. In the case with Au layer thickness, $t_{Au} = 60$ nm, for RI 1.42 , no resonance was obtained; consequently, the RI range reduces ($1.37-1.41$) along with maximum WS (12000 nm/RIU). Thus Au layer thickness, $t_{Au} = 50$ nm was considered as the optimal value for the reference structure.

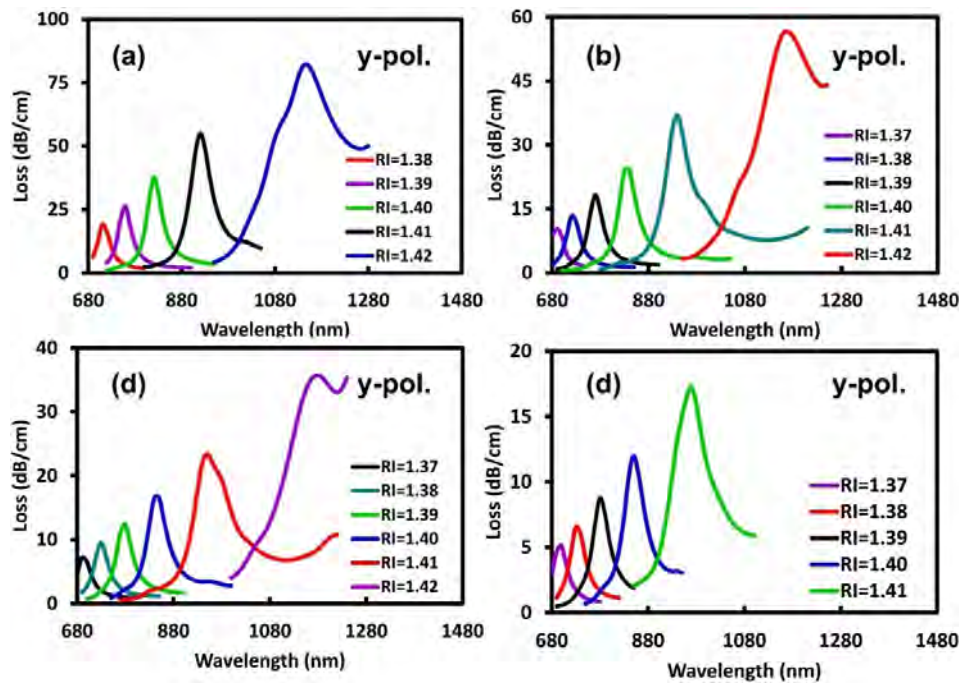


Fig. 4.2. Variation of Au layer thickness on the reference structure. (a) CL spectra for $t_{Au} = 45$ nm for RI range of $1.38-1.42$. (b) CL spectra for $t_{Au} = 50$ nm for RI range of $1.37-1.42$. (c) CL spectra for $t_{Au} = 55$ nm for RI range of $1.37-1.42$. (d) CL spectra for $t_{Au} = 60$ nm for RI range of $1.38-1.41$.

4.4 Optimization of distances between adjacent air-holes (d_3)

The distance between adjacent air-holes was varied to see the impact on the reference structure and to find the optimal distance while keeping the core diameter unchanged. As such, distance, $d_3 = 1.5, 2.0$ and $2.5 \mu\text{m}$ was varied while keeping the pitch $\Lambda = 2 \mu\text{m}$, Au layer thickness, $t_{\text{Au}} = 50 \text{ nm}$, larger air-hole diameter $d_1 = 1.0 \mu\text{m}$, and smaller air-hole diameter $d_2 = 0.5 \mu\text{m}$ as fixed. The consequence of varying distance between adjacent air-holes on CL is plotted as a function of wavelength for RI of 1.41-1.42 for y-polarized modes, as shown in **Fig. 4.3**. With the distance between adjacent air-holes, $d_3 = 1.5 \mu\text{m}$, the sensor achieves the maximum WS of 23000 nm/RIU with a RI range of 1.37-1.42. The sensor performs better with the distance, $d_3 = 2.0 \mu\text{m}$ as it shows the maximum WS of 27000 nm/RIU but at the cost of the sensor's reduced RI range (1.38-1.42). With distance, $d_3 = 2.5 \mu\text{m}$, the maximum WS (34000 nm/RIU) increases further but at the higher cost of the sensor's reduced RI range (1.39-1.42). RI range of the reference structure is significant because it would contribute to the RI range of multi-channel with multi-analyte sensor. Thus considering the RI range distance between adjacent air-holes, $d_3 = 1.5 \mu\text{m}$ was considered as the optimal distance.

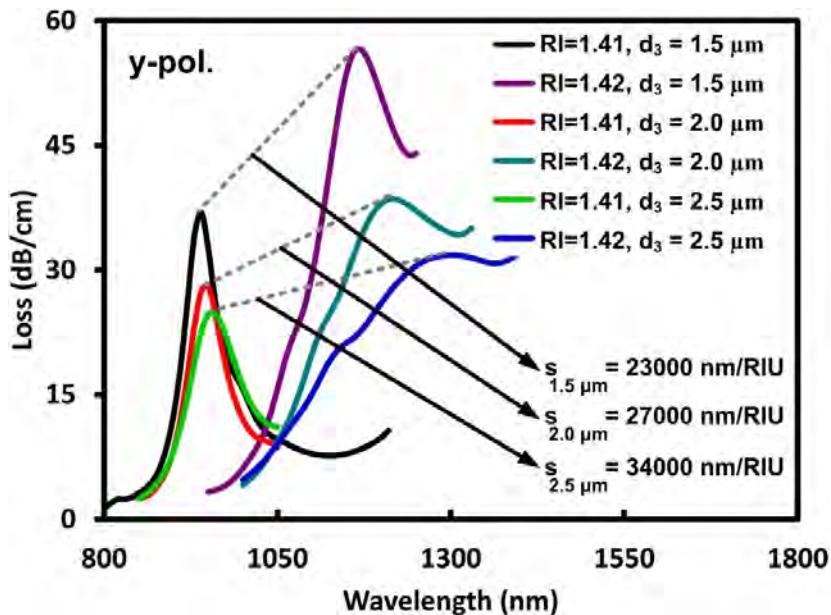


Fig. 4.3. Effect of variation of distance between adjacent air-holes, d_3 . Plot showing CL spectra for $d_3 = 1.5, 2.0$ and $2.5 \mu\text{m}$ for RI of 1.41-1.42

4.5 Summary

Chapter 4 describes the step by step optimization of the sensor's basic structure. This optimized structure will serve as the reference structure. In the next chapter channel specific optimization will be carried out where the parameters of the reference structure will be used. In the process of reference structure optimization, initially pitch was optimized followed by diameters of the air-holes. Finally Au layer thickness (t_{Au}) and distances between air-holes (d_3) were optimized. In the next chapter different channels of sensor will be optimized.

Chapter 5

Multi-channel Optimization

5.1 Preferred state of polarization and SPP mode selection

In the process of simulation it was found that both x and y-polarization is exhibited. Both the modes can be utilized to find out the performance of the sensor. However, investigating and studying the both polarization a bit time consuming. By observing the CL plots, it is possible to decide the preferred mode of polarization. In the actual sensing operation with optical spectral analyzer and computer connected with it, CL and state of polarization are very important. Because, if the resonance peak is not that sharper it will be blurred within the other associated noise. **Fig. 5.1** shows the CL profiles for x and y-polarization modes for the three channels. Due to the geometric position of Au film in channel-1, the y-polarization state is stronger than x-polarization as shown in **Fig. 5.1 (a)**. Consequently, loss peak is more prominent in y-polarization than x-polarization in channel-1. As a result, the SPR effect excited by the coupling of the core mode and the SPP mode will be stronger in y-polarization than in x-polarization. Similarly, due to positional polarization states of metal (Au) and oxide layers (Ta_2O_5 and TiO_2), loss peaks (see **Fig. 5.1 (b) to (c)**) related to y and x-polarization are more prominent in channel-2 and channel-3, respectively. It is because of arrangement of air-holes, position of channels, plasmonic material coatings in the channels and the structural design of the sensor. Thus, considering the coupling efficiency due to polarization advantage, y, y and x-polarization will be utilized for channel-1, channel-2, and channel-3, respectively for further study.

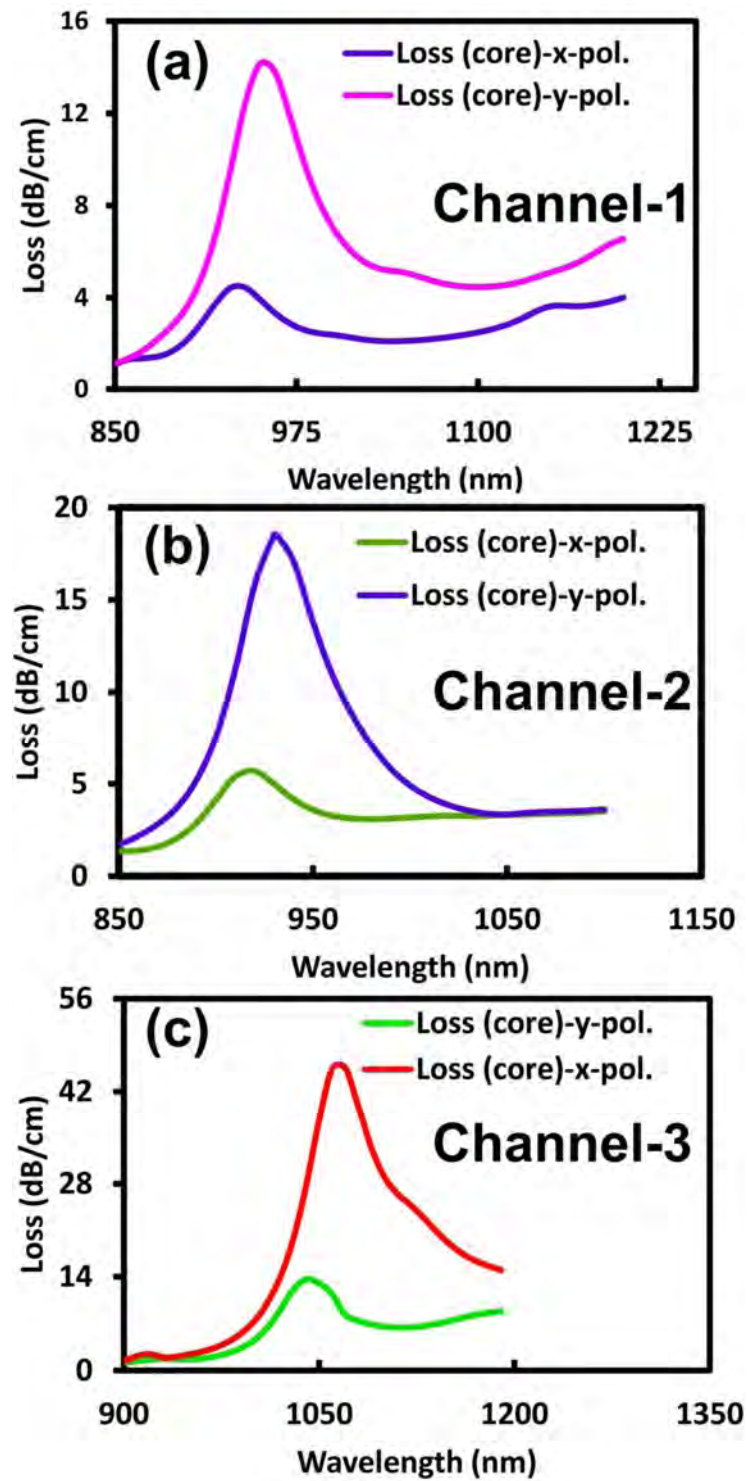


Fig. 5.1. State of polarization (x and y) and associated loss spectra. (a) – (c) CL spectra for $n_a = 1.41$ for channel-1, 2 and 3 respectively.

As shown in Fig. 5.2 (a) to (c) that there exists a first-order SPP mode (SPP-1), a second-order SPP mode (SPP-2), and a third-order SPP mode (SPP-3). Fig. 5.2 (d) shows the SPP modes analysis. The imaginary part of the effective index to which core mode CL is proportional is also included in the figure and shown as red color. The effective index of the SPP-3 mode (light green color) is much lower and it does not interact with the core mode, and hence it can never couple to it and thus be discarded. SPP-1 (violet color) interacts with the core mode but does not represent any CL peaks, and it is not distinguishable. SPP-2 (sky blue) mode and core mode interact and match at the wavelength of 950 nm. Consequently, CL peaks appear at 950 nm. Thus, in further study, the SPP-2 mode will be utilized.

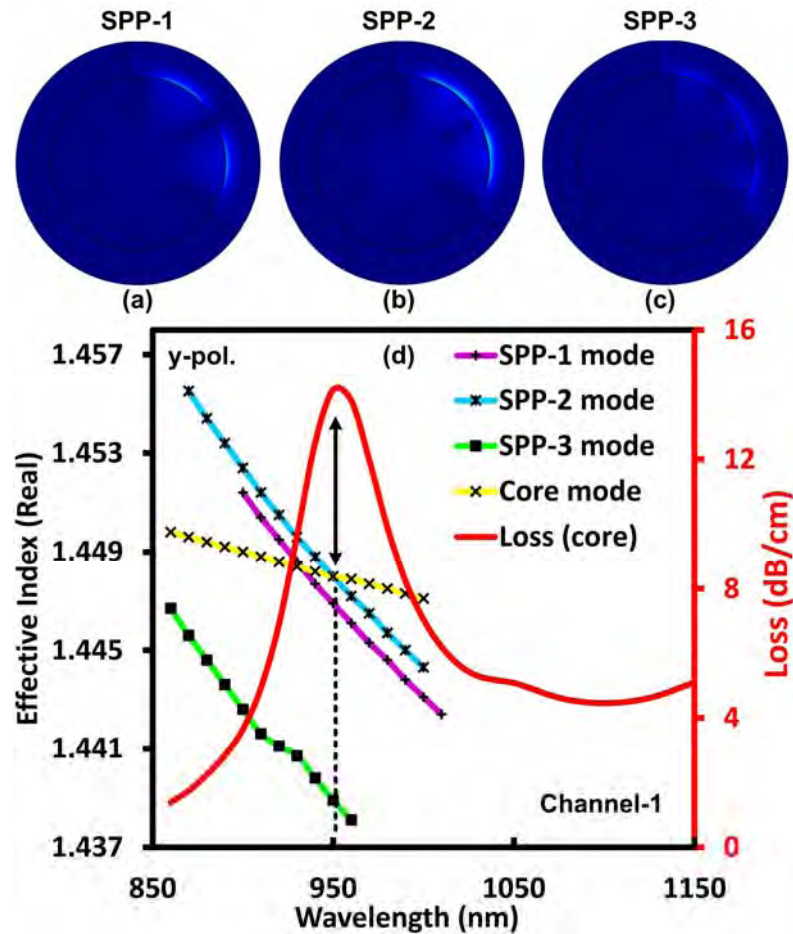


Fig. 5.2. SPP modes analysis for channel-1. (a) SPP-1 mode. (b) SPP-2 mode. (c) SPP-3 mode. (d) Interaction of y-polarized core mode with different SPP modes.

5.2 Optimization of Channel-1(With Au)

The investigation started with the metal thickness for channel-1 at $t_{Au} = 45$ nm. As a general trend, increasing the Au layers increases the WS. However, increasing the Au layer thickness beyond $t_{Au} = 55$ nm, decreases the WS and FOM. **Table 5.1** summarizes all quality parameters for varying the Au layer thickness for channel-1. As it can be seen from **Table 5.1** that, performance with Au layer, $t_{Au} = 55$ nm is quite distinctive considering maximum WS, average WS, maximum FOM, average FOM, and RI range. Thus, Au layer thickness, $t_{Au} = 55$ nm is the optimal value for channel-1. **Fig. 5.3** illustrates the effect of varying thicknesses on the CL.

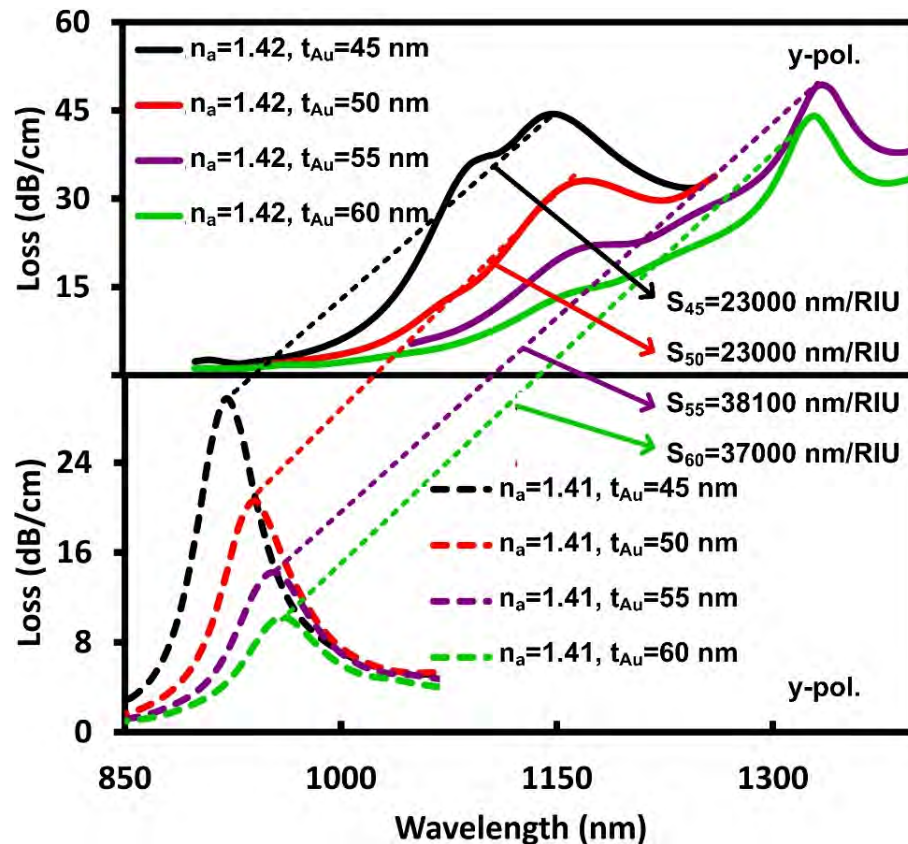


Fig. 5.3. Variation of Au layer thickness, t_{Au} in the channel-1 of the proposed multi-channel and multi-analyte sensor.

TABLE 5.1. PERFORMANCE PARAMETERS FOR VARYING Au LAYER THICKNESS

Au Layer Thickness (t_{Au})	Max. CL (dB/cm)	Max. WS (nm/RIU)	Avg. WS (nm/RIU)	Max. FOM (RIU^{-1})	Avg. FOM (RIU^{-1})	RI Range (RIU)
45 nm	44.364	23000	11000	460	272	1.37-1.42
50 nm	33.03	23000	11250	383	258.33	1.38-1.42
55 nm	49.535	38100	15125	635	274.85	1.37-1.42
60 nm	43.984	37000	12600	462.5	232.28	1.37-1.42

5.3 Optimization Inter-channel gap (d_g)

The gap between channels, d_g has an impact on the performance of the sensor. The gap between the channels was varied as, $d_g = 1.0, 1.5$ and $2.0 \mu m$ to find the optimal value. It can be seen in **Table 5.2** that with the increase of the gap between channels, FOM and AS deteriorate. Because an increase in channel gap not only decreases the plasmonic layers, but also shrinks the analyte channels. Furthermore, with the increase in channel gap, average WS, maximum AS, and the RI range decreases. Thus, the gap between channels, $d_g = 1.0 \mu m$ was selected as the optimal value. This value would be used for further investigation for channel-2 and channel-3 of the proposed sensor.

TABLE 5.2. PERFORMANCE PARAMETER AS A RESULT OF VARYING INTER CHANNEL GAP (d_g)

Gap between channels (d_g)	Max. WS (nm/RIU)	Avg. WS (nm/RIU)	Max. FOM (RIU^{-1})	Avg. FOM (RIU^{-1})	Max. AS (RIU^{-1})	RI Range (RIU)
1.0 μm	38100	15125	635.00	308.75	-582.68	1.37-1.42
1.5 μm	38100	15100	544.28	283.98	-579.45	1.38-1.42
2.0 μm	38100	15025	544.28	260.44	-576.85	1.38-1.42

5.4 Optimization of Channel-2 (With Au and Ta₂O₅)

The plasmonic materials of channel-2 are Au and Ta₂O₅. Total eight combinations of Au and Ta₂O₅ layer thickness variations were investigated to find the optimal layers in channel-2. All important findings on the thickness optimization of channel-2 are tabulated in **Table 5.3**. The investigation started with Au layer thickness, $t_{Au} = 35$ nm along with a layer of Ta₂O₅, $t_{Ta_2O_5} = 15$ nm. As a general pattern, it was observed that the increasing Au layer thickness increases the WS. However, increasing the Au layer thickness beyond 50 nm reduces the WS. It can be seen that all the thickness combinations do not result same RI range. Wider RI range should be given preference because it will cover more analyte sample. As it can be seen from the Table 5.3 that with $t_{Au} = 50$ nm and $t_{Ta_2O_5} = 10$ & 15nm, the sensor achieves same wide RI range. However, with $t_{Au} = 50$ nm and $t_{Ta_2O_5} = 10$ nm the sensor achieves better WS. Again, CL is an important parameter which has impact on the performance of the sensor. Considering the wide RI range, minimum CL, maximum WS $t_{Au} = 50$ nm and $t_{Ta_2O_5} = 10$ nm were found to be optimal layers for channel-2.

TABLE 5.3. PERFORMANCE PARAMETERS AS A RESULT OF VARYING Au AND Ta₂O₅ LAYER THICKNESSES

Au Thickness	Ta₂O₅ Thickness	Max. CL (dB/cm)	Max. WS (nm/RIU)	RI Range (RIU)
35 nm	15 nm	91.978	12000	1.39-1.42
40 nm	10 nm	60.672	16000	1.38-1.42
40 nm	15 nm	58.732	15000	1.39-1.42
40 nm	20 nm	56.508	14000	1.39-1.42
45 nm	10 nm	36.487	17000	1.38-1.42
45 nm	15 nm	36.76	16000	1.38-1.42
50 nm	10 nm	28.289	21600	1.37-1.42
50 nm	15 nm	26.552	20400	1.37-1.42

5.5 Optimization of Channel-3 (With Au and TiO_2)

Channel-3 was designed with Au and TiO_2 . The plasmonic layers in this channel were optimized by varying the thicknesses. As it can be seen from **Table 5.4**, a total of eight combinations of Au and TiO_2 layer thicknesses were investigated to find the best combination. Initially, it was considered the findings with a broader RI range (1.36-1.42), and then priority was given to the maximum WS, and maximum FOM. From the **Table 5.4**, it is clear that channel-3 performs best with Au layer thickness, $t_{Au} = 45$ nm and TiO_2 layer thickness, $t_{TiO_2} = 10$ nm. With this thickness combination, channel-3 also achieves remarkable performance in the case of AS. Thus for channel-3, Au layer thickness, $t_{Au} = 45$ nm and TiO_2 layer thickness, $t_{TiO_2} = 10$ nm combination is the optimal values.

TABLE 5.4. PERFORMANCE PARAMETERS AS A RESULT OF VARYING AU AND TiO_2 LAYER THICKNESSES

Au Thickness	TiO_2 Thickness	Max. CL (dB/cm)	Max. WS (nm/RIU)	Max. FOM (RIU^{-1})	Max. AS (RIU^{-1})	RI Range (RIU)
35 nm	15 nm	187.79	29000	966.66	-2503.84	1.36-1.42
40 nm	10 nm	92.31	34000	680.00	-1666.08	1.36-1.42
40 nm	15 nm	92.278	14000	466.66	-1462.19	1.36-1.41
45 nm	10 nm	88.956	45800	572.50	-1230.08	1.36-1.42
45 nm	15 nm	55.941	18000	450.00	-1142.87	1.36-1.41
50 nm	10 nm	60.30	43000	450.00	-965.52	1.36-1.42
50 nm	15 nm	39.085	17000	340.00	-945.11	1.36-1.41
55 nm	10 nm	41.50	37000	375.00	-669.22	1.36-1.42

5.6 Summary

This chapter describes multi-channel optimization. Initially the preferred polarization mode selection and desired SPP mode selection was done. Later plasmonic materials in three channels were optimized. Next chapter describes the results obtained and its chronological discussion.

Chapter 6

Result and Discussion

6.1 Optimized parameters

After detailed investigation of all the parameters, the optimized common structural parameters for three channels are $\Lambda = 2.0 \mu\text{m}$, $d_1 = 1.0 \mu\text{m}$, $d_2 = 0.5 \mu\text{m}$, $d_3 = 1.5 \mu\text{m}$, $d_4 = 3.5 \mu\text{m}$, and $d_g = 1.0 \mu\text{m}$. Besides, the channel-specific optimized parameters are, $t_{\text{Au}} = 55 \text{ nm}$ (channel-1), $t_{\text{Au}} = 50 \text{ nm}$ and $t_{\text{Ta}_2\text{O}_5} = 10 \text{ nm}$ (channel-2), and $t_{\text{Au}} = 45 \text{ nm}$ and $t_{\text{TiO}_2} = 10 \text{ nm}$ (channel-3).

6.2 Phase-matching and Dispersion curve analysis

With these optimized parameters for the proposed sensor, **Fig. 6.1 (a) to (c)** shows the dispersion relations for $n_a = 1.41$ for channel-1, channel-2, and channel-3, respectively. Due to the different specific geometric positions of the plasmonic layer in the channels, one polarized mode is stronger than the other. Thus in the study of optimized sensor performance, y-polarization will be considered in channel-1 and channel-2. In the case of channel-3, x-polarization was considered. From the dispersion relation, it can be seen that phase matching has been established. The wavelengths where core-guided modes and SPP modes are phase-matched, are indicated with a dotted line (from the intersection point down to the horizontal axis). At this point, the wave vectors of the two modes are equal, and a sharp CL peak appears because the plasma absorbs maximum core energy.

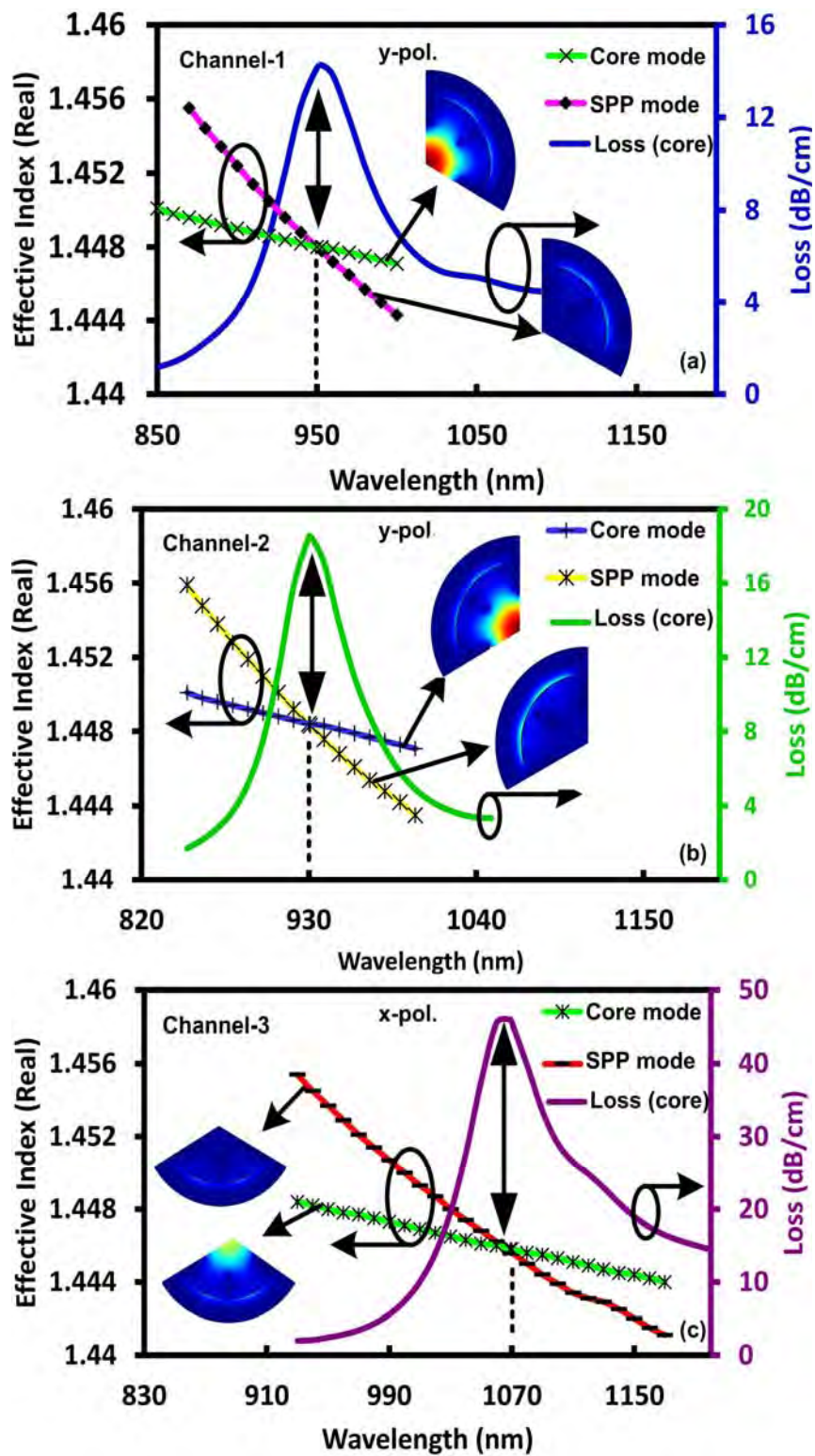


Fig. 6.1. Sensor's wavelength-dependent dispersion relation for SPP mode and core-guided mode, for $n_a = 1.41$. (a) Channel-1 with y-polarization. (b) Channel-2 with y-polarization. (c) Channel-3 with x-polarization.

6.3 CL Analysis

Proposed sensor exhibits much lower loss. CL is related to the length of the sensor. Lower the CL it is better for the realization. In the case of channel-1, the lowest CL 3.8071 dB/cm is achieved for RI 1.37. For channel-2, CL of 5.2678 is achieved by for RI of 1.37. For RI of 1.36 for channel-3, CL of 10.62 dB/cm is achieved. Highest CLs of 49.535 dB/cm (channel-1), 28.289 dB/cm (channel-2) and 88.956 dB/cm (channel-3) achieved by the three channels of the multi-channel and multi-analyte sensor are much lower than other multi-channel sensors those are reported previously[1-3, 6-9, 12, 29].

6.4 Wavelength Sensitivity Analysis

For channel-1 for y-polarized mode, when RI changes from 1.37 to 1.38, 1.38 to 1.39, 1.39 to 1.40, 1.40 to 1.41 and 1.41 to 1.42 sensor achieves WS of 3900, 4800, 6700, 10900 and 38100 nm/RIU respectively. For channel-2 for y-polarized mode, when RI changes from 1.37 to 1.38, 1.38 to 1.39, 1.39 to 1.40, 1.40 to 1.41 and 1.41 to 1.42 sensor achieves WS of 2900, 4400, 6200, 9600 and 21600 nm/RIU respectively. For channel-3 for x-polarized mode, when RI changes from 1.36 to 1.37, 1.37 to 1.38, 1.38 to 1.39, 1.39 to 1.40, 1.40 to 1.41 and 1.41 to 1.42 sensor achieves WS of 3400, 4300, 6000, 7900, 13300 and 45800 nm/RIU respectively. For channel-1, the resonance peak appears at 690, 729, 777, 844, 953, and 1334 nm for RI of 1.37, 1.38, 1.39, 1.40, 1.41 and 1.42 respectively. For channel-2, the resonance peak appears at 700, 729, 773, 835, 931, and 1147 nm for RI of 1.37, 1.38, 1.39, 1.40, 1.41 and 1.42 respectively. For channel-3, the resonance peak appears at 720, 754, 797, 857, 936, 1069, and 1527 nm for RI of 1.36, 1.37, 1.38, 1.39, 1.40, 1.41 and 1.42 respectively. To summarize, the proposed sensor achieves maximum WS of 38100 nm/RIU, 21600 nm/RIU, and 45800 nm/RIU for channel-1, channel-2, and channel-3, respectively. Achieved maximum WS of the proposed multi-channel and multi-analyte sensor as per channels is much higher than the multi-analyte sensor previously reported in [1-3, 6-9, 12, 29]. For practical sensing average WS is very important. Proposed sensor achieves average WS of 12880 nm/RIU, 8940 nm/RIU and 13450 nm/RIU for channel-1, channel-2 and channel-3, respectively which also much higher than many sensors. CL plots for channel-1, channel-2 and channel-3 are depicted in **Fig. 6.2**.

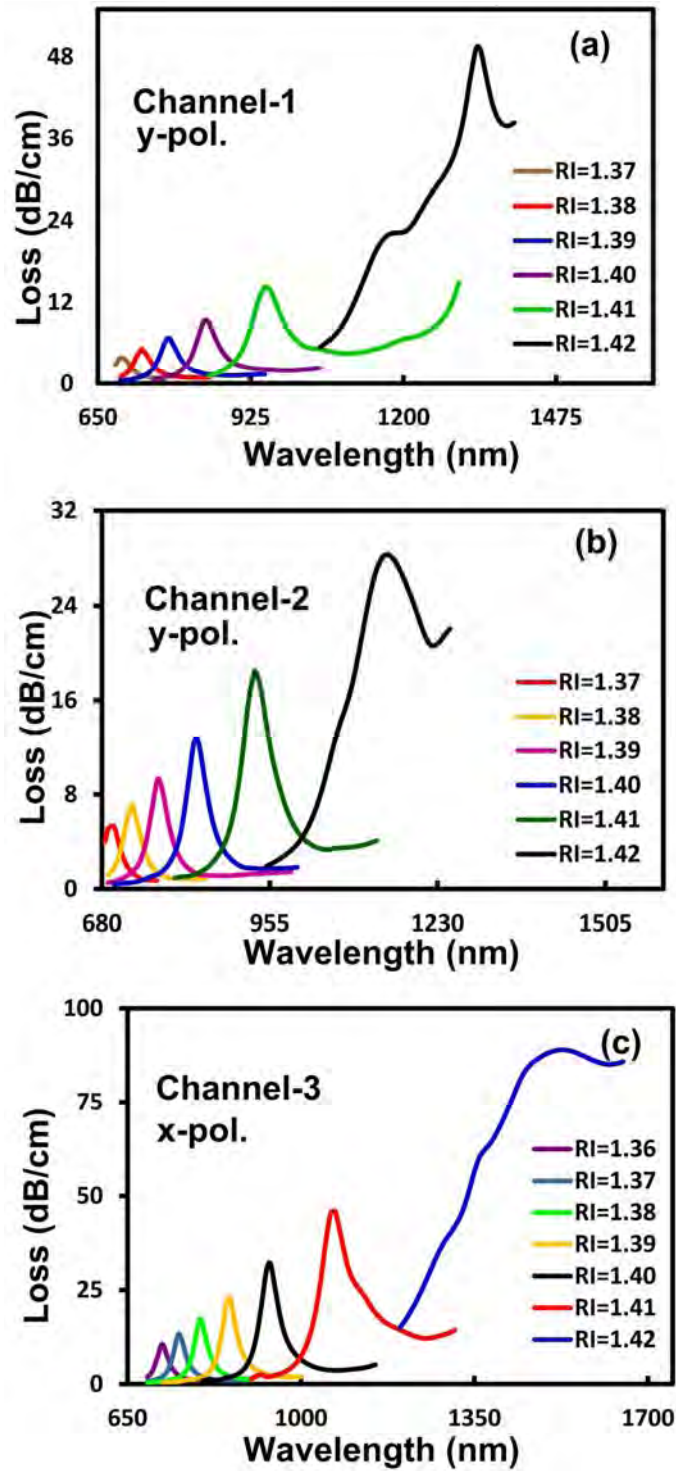


Fig. 6.2. CL plots for the optimized sensor. (a) Channel-1 for RI of 1.37-1.42. (b) Channel-2 for RI of 1.37-1.42. (c) Channel-3 for RI of 1.36-1.42.

6.5 Amplitude Sensitivity Analysis

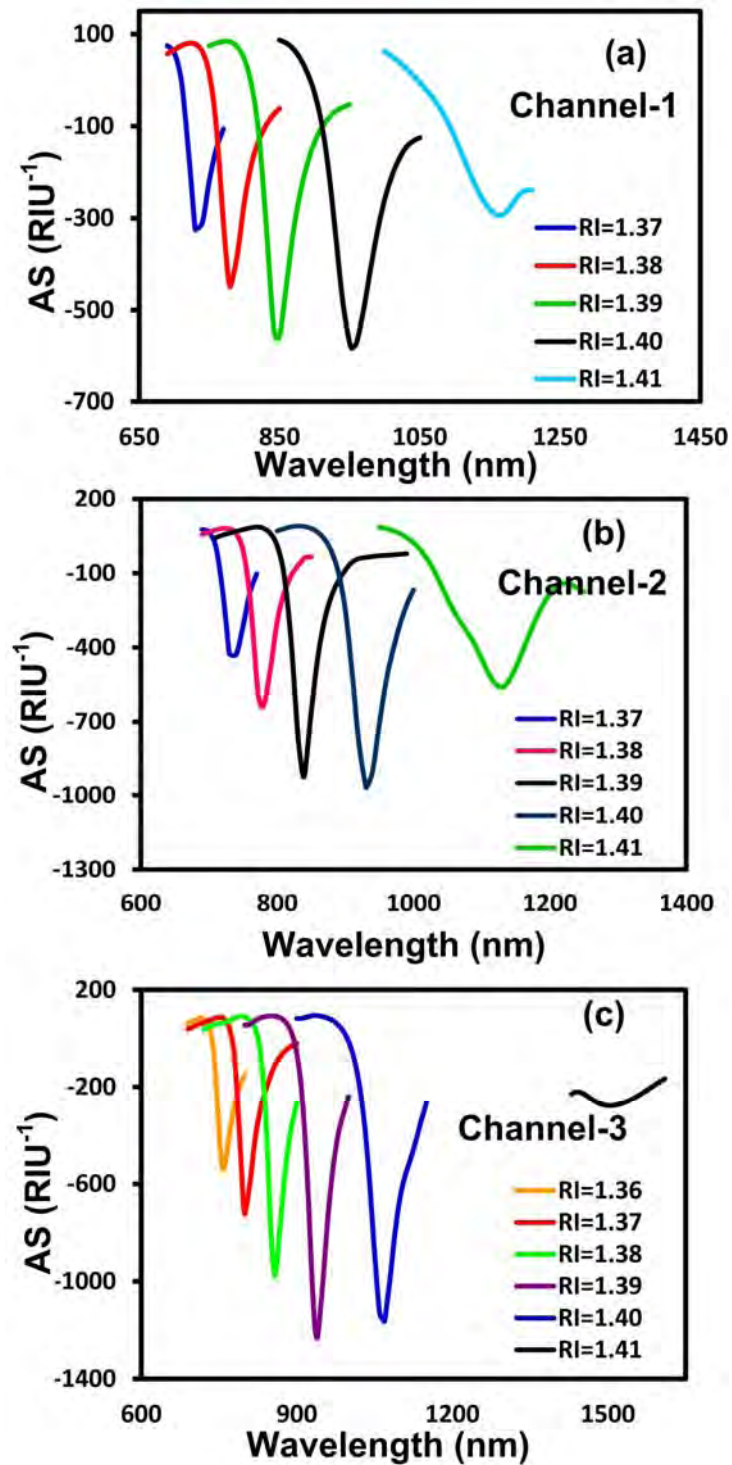


Fig. 6.3. AS spectra for the optimized sensor. (a) Channel-1 for RI of 1.37-1.41. (b) Channel-2 for RI of 1.37-1.41. (c) Channel-3 for RI of 1.36-1.41.

For channel-1 and for y-polarization, AS of 324.75, -448.40, -558.28, -582.68, and -293.51 RIU⁻¹ achieved for RI of 1.37, 1.38, 1.39, 1.40 and 1.41 respectively. For channel-2 and for y-polarization, AS of -427.14, -635.54, -919.48, -969.57, and -561.27 RIU⁻¹ achieved for RI of 1.37, 1.38, 1.39, 1.40 and 1.41 respectively. For channel-3 and for x-polarization, AS of -536.69, -722.29, -975.40, -1230.08, -1163.75, and -191.84 RIU⁻¹ achieved for RI of 1.36, 1.37, 1.38, 1.39, 1.40 and 1.41 respectively. In the case of AS, the sensor achieves a maximum AS of 582.68 RIU⁻¹, 969.57 RIU⁻¹, and 1230.08 RIU⁻¹ for channel-1, channel-2, and channel-3, respectively. Channel-specific performance in the AS is quite distinctive and better than those are reported previously in [7, 8, 29]. **Fig. 6.3** shows the AS plots for the three channels.

6.6 Sensor Resolution

For channel-1 and for y-polarization, for RI of 1.37, 1.38, 1.39, 1.40 and 1.41, the sensor achieves wavelength resolution of 2.56×10^{-5} , 2.08×10^{-5} , 1.49×10^{-5} , 9.17×10^{-6} , and 2.62×10^{-6} RIU respectively. For channel-2 and for y-polarization, for RI of 1.37, 1.38, 1.39, 1.40 and 1.41, the sensor achieves wavelength resolution of 3.45×10^{-5} , 2.27×10^{-5} , 1.61×10^{-5} , 1.04×10^{-5} , and 4.63×10^{-6} RIU respectively. For channel-3 and for x-polarization, for RI of 1.36, 1.37, 1.38, 1.39, 1.40 and 1.41, the sensor achieves wavelength resolution of 2.94×10^{-5} , 2.33×10^{-5} , 1.67×10^{-5} , 1.27×10^{-5} , 7.52×10^{-6} , and 2.18×10^{-6} RIU respectively. Similarly, proposed sensor achieves maximum wavelength resolution for the three channels are 2.62×10^{-6} RIU (channel-1), 4.63×10^{-6} RIU (channel-2), and 2.18×10^{-6} (channel-3) also much lower than the previously reported sensors. For channel-1 and for y-polarization, for RI of 1.37, 1.38, 1.39, 1.40 and 1.41, the sensor achieves amplitude resolution of 3.08×10^{-5} , 2.23×10^{-5} , 1.97×10^{-5} , 1.72×10^{-5} , and 3.41×10^{-5} RIU respectively. For channel-2 and for y-polarization, for RI of 1.37, 1.38, 1.39, 1.40 and 1.41, the sensor achieves amplitude resolution of 2.34×10^{-5} , 1.57×10^{-5} , 1.09×10^{-5} , 1.03×10^{-5} , and 1.78×10^{-5} RIU respectively. For channel-3 and for x-polarization, for RI of 1.36, 1.37, 1.38, 1.39, 1.40 and 1.41, the sensor achieves amplitude resolution of 1.86×10^{-5} , 1.38×10^{-5} , 1.03×10^{-5} , 8.13×10^{-6} , 8.59×10^{-6} , and 5.21×10^{-5} RIU⁻¹ respectively.

In the case of maximum amplitude resolution for channel-1, channel-2, and channel-3, the sensor achieves 1.72×10^{-5} RIU, 1.03×10^{-5} RIU and 8.13×10^{-6} RIU, respectively.

6.7 FOM Analysis

From **Table 6.1**, it can be seen that as a general trend, FOM increases with the increase in RI. The proposed sensor achieves a maximum FOM of 635 RIU^{-1} , 432 RIU^{-1} , and 572.5 RIU^{-1} for channel-1, channel-2, and channel-3, respectively. All the maximum FOMs in the three channels are higher than those sensors previously reported[7].

6.8 Summary of Important Data

Important data related to the sensor characteristics is appended below in **Table 6.1**.

TABLE 6.1 SUMMARY OF SENSOR'S PERFORMANCE IN THREE CHANNELS

Ch	RI of Analyte	Pol. Mode	Reso. Wav. (nm)	Wav. Sen. (nm/RIU)	AS. RIU^{-1}	FOM RIU^{-1}
CH-1 Au	1.37	y-pol.	690	3900	324.75	139.2
	1.38	y-pol.	729	4800	448.40	160
	1.39	y-pol.	777	6700	558.28	167.5
	1.40	y-pol.	844	10900	582.68	272.5
	1.41	y-pol.	953	38100	293.51	635
	1.42	y-pol.	1334	NA	NA	NA
CH-2 Au and Ta₂O₅	1.37	y-pol.	700	2900	427.14	119
	1.38	y-pol.	729	4400	635.54	220
	1.39	y-pol.	773	6200	919.48	206.67
	1.40	y-pol.	835	9600	969.57	320
	1.41	y-pol.	931	21600	561.27	432
	1.42	y-pol.	1147	NA	NA	NA
CH-3 Au and TiO₂	1.36	x-pol.	720	3400	536.69	170
	1.37	x-pol.	754	4300	722.29	143.33
	1.38	x-pol.	797	6000	975.40	300
	1.39	x-pol.	857	7900	1230.08	263.33
	1.40	x-pol.	936	13300	1163.75	332.5
	1.41	x-pol.	1069	45800	191.84	572.5
	1.42	x-pol.	1527	NA	NA	NA

6.9 Polynomial Fitting Curve

There exists a relationship between resonance wavelength and values of target analyte RI. Expressing this relation in an analytical interpretation helps to understand the continuous relation between RI and resonance wavelength. **Fig. 6.4 (a) to (c)** depict the changing trend of the resonance wavelength as RI increases along with polynomial curve-fitting. The corresponding polynomial regression equation, the correlation coefficient, R^2 and other parameters are indicated in the respective figures for channel-1 to channel-3.

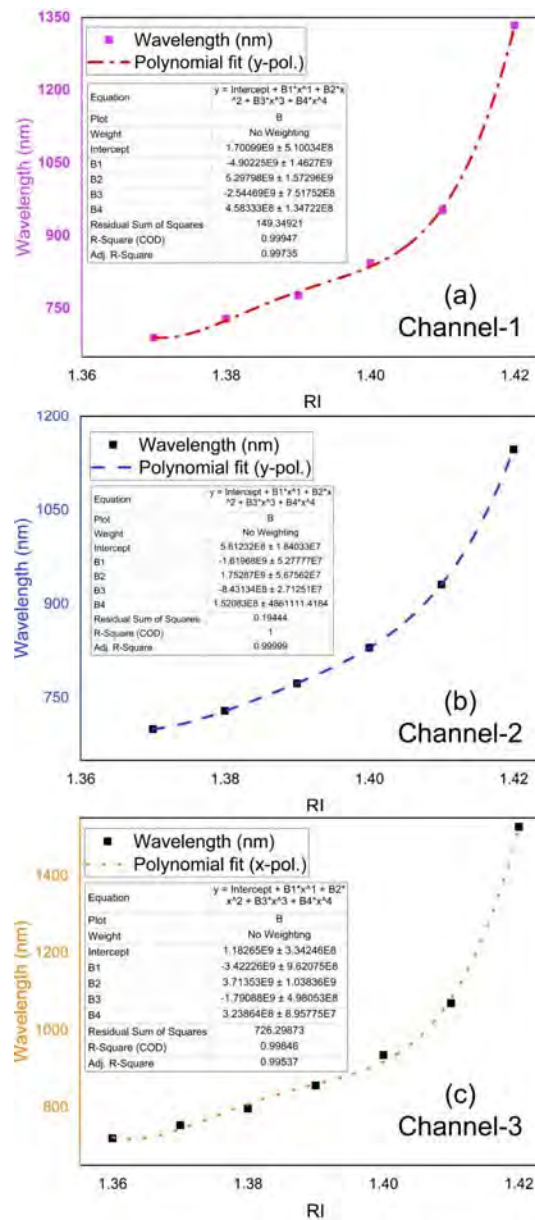


Fig. 6.4. Polynomial curve fitting. (a) For channel-1 (b) For channel-2 (c) For channel-3

6.10 Performance Comparison

The proposed sensor's performance is compared to that of previously reported multi-channel sensors. The overall RI range of the proposed sensor is from 1.36 to 1.42. The average WS of the proposed sensor, an important parameter for practical sensing, is significantly high ((12880 nm/RIU (channel-1), 8940 nm/RIU (channel-2) and 13450 nm/RIU (channel-3)). Important comparative parameters of literature reviewed multi-channel sensors and other multi-channel sensors are tabulated in Table 7 to compare with the performance of the proposed sensor. From **Table 6.2**, it is evident that the maximum CL of the proposed sensor is remarkably less which says that useable fiber length utilizing this sensor is practical. As it can be seen, from **Table 6.2**, the performance of the proposed multi-channel and multi-analyte sensor is distinctive and shows better results in the all the fields such as WS, WS resolution, AS, AS resolution FOM, and so on.

TABLE 6.2. COMPARATIVE PERFORMANCE ANALYSIS OF PROPOSED SENSOR

Description (Number of ch, material used)	RI Range	WS (nm/RIU)	AS. (RIU⁻¹)	Highest CL (dB/cm)
Two, Au and Au with a dielectric layer[1]	1.33-1.40	11600 (ch-1) 10600(ch-2)	NA	5800
Two, Au coated [2]	1.33-1.39	6100(ch-1) 2300(ch-2)	NA	775
Two, Au and Silver (Ag) [3]	1.33-1.366	2500(ch-1) 3083(ch-2)	NA	110
Four, Au, Au and Ta ₂ O ₅ [4]	1.33-1.36	2300(ch-1) 4600(ch-2)	NA	480
Two, Au [5]	1.30-1.40	1000(ch-1) 3750(ch-2)	0.5(ch-1) 40(ch-2)	5449
Two, Au and Ag [6]	1.33-1.35	4500(ch-1) 7500(ch-2),	NA	300
Three, Au coated [7]	1.33-1.35 1.36-1.38 1.39-1.42	2000(ch-1) 3000(ch-2) 18000(ch-3)	95(ch-1) 184(ch-2) 427(ch-3)	340
Four, Au [8]	1.33-1.34	2200(ch-1) 2400(ch-2), 2200(ch-3), 2400(ch-4)	-	1450
Two, Au and Ag [9]	1.33-1.37	6000(ch-1), 7000(ch-2)	-	500
Two, Au and TiO ₂ [12]	1.46-1.485	23000(ch-1)	820	818
One, Au and Graphene(experimental) [14]	1.3330-1.3688	2290	-	73
One, Au (experimental)[15]	1.3348-1.3673	2331.9	-	35
Three, Au, Au with Ta ₂ O ₅ , and Au with TiO ₂ [Our work]	1.37-1.42(ch-1)	38100(ch-1)	582.68(ch-1)	49.53(ch-1)
	1.37-1.42(ch-2)	21600(ch-2)	969.57(ch-2)	28.28(ch-2)
	1.36-1.42(ch-3)	45800(ch-3)	1230.08(ch-3)	88.95(ch-3)

6.11 Working Principle of the Proposed Sensor

The proposed sensor is spliced with the optical spectrum analyzer and optical tunable source (OTS) through single-mode fiber (SMF) for practical sensing application. With the help of a pump, the analyte inflow to and outflow from the sensor can be controlled. Interaction of analyte with incident light from OTS generates spectra in the optical spectrum analyzer, which is further analyzed and interpreted in the connected computer. The proposed sensor can work both in simultaneous and non-simultaneous detection mode. To detect unknown analytes simultaneously, the sensor needs to have a considerable gap in the resonance wavelength among the channel for the same RI. Use of different plasmonic materials (TiO_2 and Ta_2O_5) in the channel aid in creating that gap. When the sensor is operated in non-simultaneous detection, only one channel is used, and other channels are kept vacant filled with air ($\text{RI} = 1.00$). When the sensor is operated for simultaneous detection mode, all the channels are filled with different analytes. Due to the same resonance wavelength (729 nm) in channel-1 and channel-2 for RI of 1.38, the sensor will work in non-simultaneous detection mode. In the rest of the cases, the proposed sensor can operate in simultaneous mode. However, it will be very rare during actual sensing operation that all the three channels are filled with the same RI value.

6.12 Summary

This chapter discusses result of the proposed multi-channel and multi-analyte sensor. In the process of result evaluation, both wavelength and amplitude interrogation methods were employed. Besides, sensor's resolution (both wavelength and amplitude) and FOM were also calculated. To measure the merit of the proposed research work, results were compared with contemporary works related to multi-channel sensors. At the end of chapter working principle of the proposed sensor was discussed. In the next chapter, specific application of the proposed sensor will be discussed.

Chapter 7

Sensor's Application

7.1 Probable Application of the Proposed Sensor

The overall RI of the proposed sensor is from 1.36 to 1.42. As it can be seen from the **Table 7.1** that a lot of chemical, biochemical, and bio samples fall with the range of achieved RI range of the proposed sensor. Anyone of the following sample can be sensed with the proposed sensor. However, it will be prudent to use similar type of sample to get optimum benefit from the proposed sensor.

TABLE 7.1 RI (1.36-1.42) OF DIFFERENT ANALYTES FOR MULTI-CHANNEL SENSOR

List of Analyte	RI	Ref
Silicone Oil	1.393	[46]
Kerosene	1.39	[46]
Cytoplasm	1.39	[47]
Platelet	1.39	[47]
Red Blood Cell	1.40	[47]
Ethanol	1.361	[46]
Acetone	1.36	[46]
20% Glucose solution in water	1.3635	[46]
White blood cell	1.36	[29]
Haemoglobin	1.36	[29]
Liver (Human)	1.369	[46]
Sugar solution, 25%	1.3723	[46]
Acetic Acid	1.37	[46]
Propylene	1.36	[46]
Hexane	1.37	[46]
Heptane	1.38	[46]
Trichlorofluoromethane refrigerant R-11	1.37	[46]
Ethanol	1.361	[46]
Blood (Jurkat)	1.376	[48, 49]
Cervical (HeLa)	1.368	[48, 49]
Adrenal glands (PC12)	1.381	[48, 49]
Breast (MDA-MB-23)	1.385	[48, 49]
Breast (MFC-7)	1.387	[48, 49]
Skin (Basal)	1.360	[48, 49]

7.2 Specific Application - Cancerous Cell Detection

The proposed sensor may potentially be employed to detect cancer disease. Human cells are made of mostly water and protein. For example, blood plasma is composed of 90% water and 10% protein. Malignant cells have a higher refractive index than healthy cells because of more protein in the nucleus of an affected cell for fast cell division. Using the RI of healthy and infected malignant cells as a marker, this sensor is expected to detect cancer of various human cells. However, there is a possibility of false negative results using this sensor. **Table 7.2** lists down the RI of healthy and infected malignant cells of the human body along with various cancer detection sensing performances according to channel. As can be seen that, in all the cases, the proposed sensor performs remarkably. In the case of wavelength interrogation, Jurkat cell, PC-12 cell, MDA-MB-23 cell, MCF-7 cell, HeLa cell, and Basal cell achieves WS of 6700, 8000, 8000, 8000, 12000, 7700 nm/RIU, respectively. Similarly, in amplitude interrogation, Jurkat cell, PC-12 cell, MDA-MB-23 cell, MCF-7 cell, HeLa cell and Basal cell achieves AS of -646.12, -715.17, -1141.61, -1160.57, -2440.30, and -1960.32 RIU⁻¹ respectively. In the case of cancer detection, the proposed sensor achieves the highest FOM of 600 RIU⁻¹ for HeLa cell. Achieved results related to cancer detection are superior to those reported in[50, 51]. WS and AS plots related to cancerous cell detection is shown in **Fig. 7.1**.

TABLE 7.2 PERFORMANCE OF THE SENSOR IN DIAGNOSING CANCEROUS CELLS OF HUMAN BODY

Ch	Type of Cancer Cell	RI	Reso. Wav. (nm)	Loss Peak shift (nm)	WS (nm/RIU)	AS (RIU ⁻¹)
Ch-1	Blood (Jurkat)-Normal	1.376	710	Ref	6700	-646.12
	Blood (Jurkat)-Cancerous	1.390	777	67	-	-
	Adrenal glands (PC12)- Normal	1.381	730	Ref	8000	-715.17
	Adrenal glands (PC12)- Cancerous	1.395	810	800		-
Ch-2	Breast (MDA-MB-23)- Normal	1.385	760	Ref	8000	-1141.61
	Breast (MDA-MB-23)- Cancerous	1.399	840	80	-	-
	Breast (MCF-7)- Normal	1.387	750	Ref	8000	-1160.57
	Breast (MCF-7)- Cancerous	1.401	830	80	-	-
Ch-3	Cervical (HeLa)- Normal	1.368	750	Ref	12000	-2440.30
	Cervical (HeLa)- Cancerous	1.392	870	120	-	-
	Skin (Basal)- Normal	1.360	720	Ref	7700	-1960.32
	Skin (Basal)- Cancerous	1.380	797	77	-	-

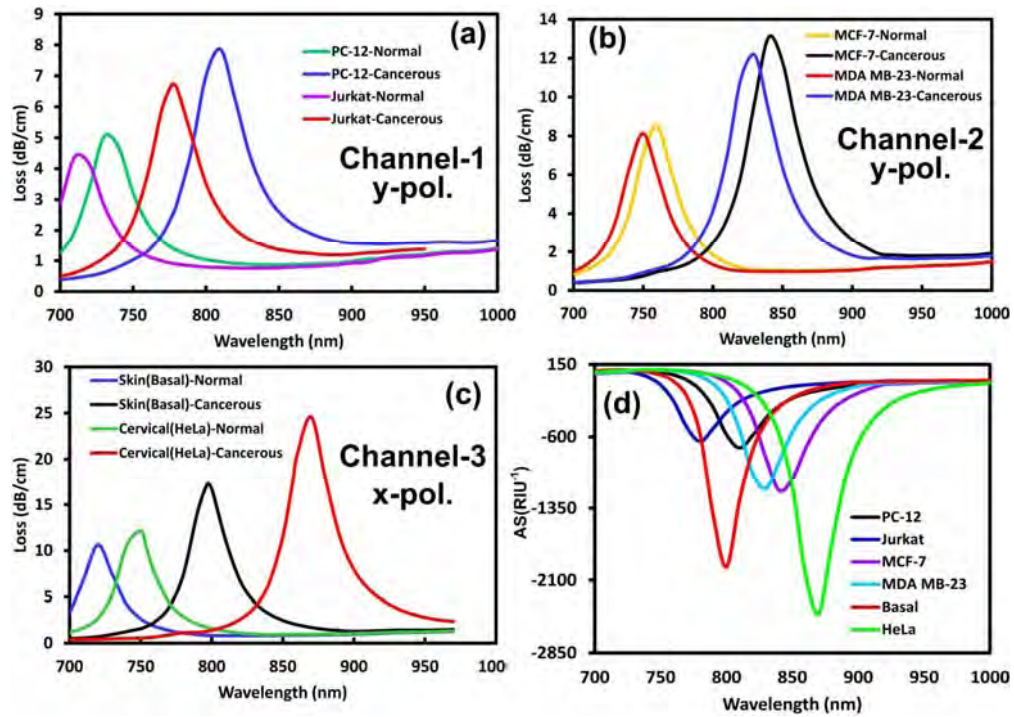


Fig. 7.1. CL and AS spectra for the cancerous cell detection. (a) CL plots for healthy and cancerous Jurkat and PC-12 cell in Channel-1. (b) CL plots for healthy and cancerous MCF-7 and MDA-MB-23 cell in Channel-2 (c) CL plots for healthy and cancerous Basal and HeLa cell in Channel-3. (d) AS plots for PC-12, Jurkat, MCF-7, MDA-MB-23, Basal and HeLa cells.

7.3 Summary

This chapter discussed the specific application of the proposed multi-channel and multi-analyte sensor. Initially a list of analyte was presented which can be sensed with the help of the proposed sensor. Later from that list, a group of similar analyte (various cancerous cells of human body) was chosen to sense with the help of proposed multi-channel and multi-analyte sensor. Next chapter discusses the fabrication feasibility of the proposed sensor.

Chapter 8

Fabrication Feasibility of the Sensor

8.1 Fabrication Tolerance Test

It is nearly impossible to fabricate the PCF SPR sensor with its exact structural parameters. Usually, $\pm 1\%$ deviation from the desired structural parameter values may take place during fabrication [52]. The proposed sensor is tested with -5% to $+5\%$ variation from the optimized parameters (d_1 , d_g , Λ , d_2 and t_{Au}) for channel-1 and for RI of 1.41. It can be noticed from **Fig. 8.1** that the sensor has a good tolerance level.

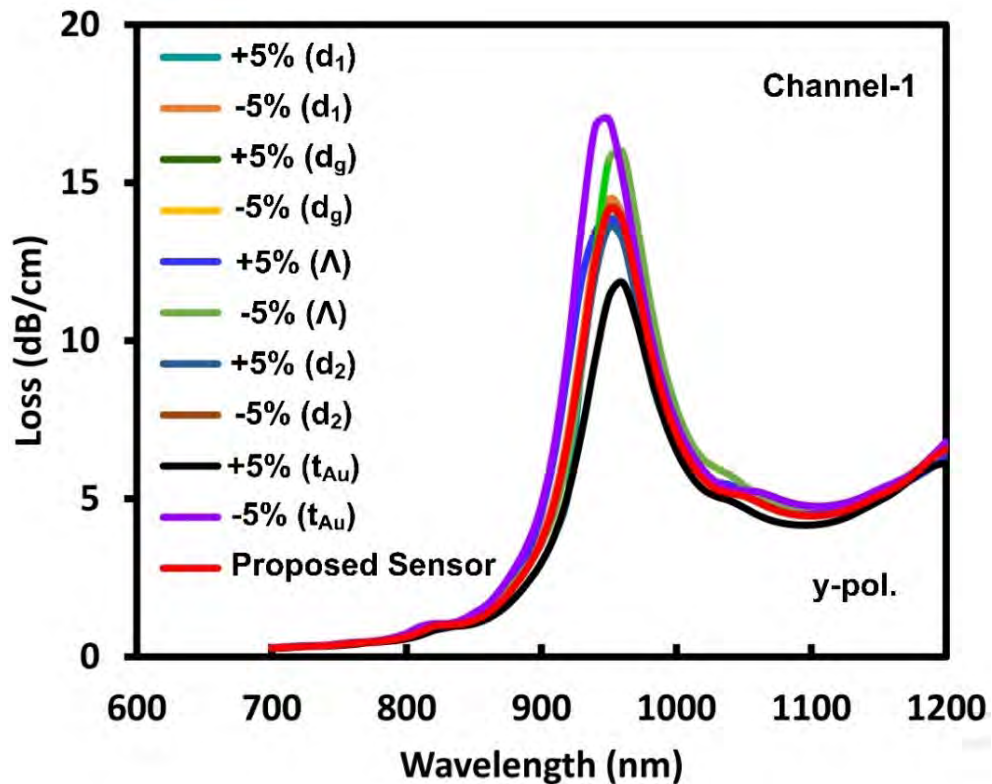


Fig. 8.1. CL loss profile for -5% to $+5\%$ variation in structural parameters such as, d_1 , d_g , Λ , d_2 and t_{Au} for RI of 1.41 in channel-1. In addition, loss curve (red color) is shown for RI of 1.41 of proposed sensor for channel-1.

8.2 Fabrication Steps of the Proposed Sensor

PCF of the proposed sensor can be fabricated with several techniques such as stack-and-draw[53], sol-gel casting[54], injection molding[55], and die-cast process[56]. However, the standard stack-and-draw technique offers many advantages such as lower cost, faster production, cleaner fabrication, and more flexibility[57]. In this method at first thick solid silica rods are drawn to make thinner silica rods. The same thick silica rods are drilled to form capillaries and then drawn to make thinner capillaries. The size of the

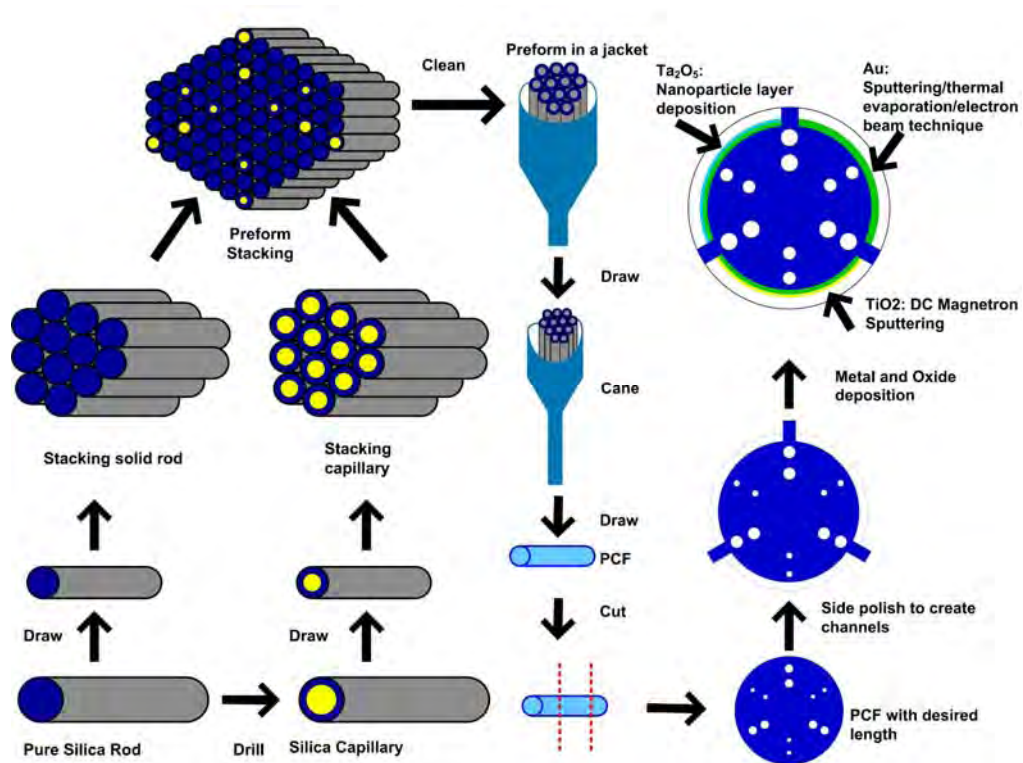


Fig. 8.2. Illustrations showing step-by-step stack-and-draw method for fabricating proposed multi-analyte and multi-channel sensor.

capillaries is controlled by feeding rate and drawing speed. Usually, capillaries are cut into 11 to 15 inches in lengths for preform. Capillary ends are sealed at one end to remove interstitial holes. Before staking the capillaries inside a jacket tube, the outer wall of capillaries needs to be cleaned by acetone followed by iso-propanol (IPA) using lint-free tissues. Cleaned capillaries are then stacked in a jacket tube using a pair of hexagonal jigs in the shape of a desired lattice. The capillary stack is moved from the short jacket tube into a longer one. A glass handle is normally attached to the preform with the help of a high-temperature $H_2 - O_2$ fuel burner. Preform is passed through silica softening

temperature ($1500^{\circ} - 17,00^{\circ}$ C) several times to get it softened. The preform is then pulled down to a cane scale. To fabricate PCF with different core size and lattice distance, another glass tube is used to jacket the cane. By carefully controlling temperature and speed of the drawing tower, preferred sizes of the fibers are made at this stage. If the size of the air-holes and lattice distance need to be corrected, then it is done by further jacketing. Finally, the cane is produced and cut according to the desired length [57]. Three analyte channels can be developed with the help of the side polishing technique [58]. Finally, Au can be deposited on the three channels of the sensor using several methods, for example, sputtering, thermal evaporation, and electron beam technique[59]. Over the Au layer, Ta_2O_5 layer in channel-2 may be deposited by nanoparticle layer deposition method[60]; TiO_2 layer in channel-3 may be deposited with the help of a DC magnetron sputtering system[33].

8.3 Summary

This chapter discusses the fabrication feasibility of the proposed multi-channel and multi-analyte sensor. To test the stability of the simulated designed $\pm 5\%$ tolerance test was carried out for the different structural parameters. The test was found quite stable. Later, some fabrication techniques were discussed to realize the proposed sensor. Next chapter will conclude the thesis.

Chapter 9

Conclusion and Future Works

9.1 Conclusion

In conclusion, a highly sensitive multi-channel and multi-analyte PCF-SPR sensor with Au (channel-1), Au with Ta₂O₅ (channel-2), and Au with TiO₂(channel-3) materials is designed and analyzed in the visible to Near Infrared wavelength region. Channel-1 (Au) achieves a WS of 38100 nm/RIU, AS of -582.68 RIU⁻¹ and a FOM of 635 RIU⁻¹. Channel-2 (Au with Ta₂O₅) achieves a maximum WS of 21600 nm/RIU, maximum AS of -969.57 RIU⁻¹ and an FOM of 432 RIU⁻¹. Channel-3 achieves a maximum WS of 45800 nm/RIU, maximum AS of -1230.08 RIU⁻¹ and an FOM of 572.5 RIU⁻¹. These values supersede previously reported multi-channel and multi-analyte sensors and guarantee better performance. Additionally, for cancer detection, in case of HeLa cell sensor achieves WS of 12000 nm/RIU, AS of -2440.30 RIU⁻¹ and a FOM of 600 RIU⁻¹. Furthermore, the reported sensor offers many advantages, such as, better sensitivity performance in all three channels, lower cost, reusability, external sensing approach with large-analyte channels, simple manufacturing potential, etc. Thus, the proposed sensor proves itself as a promising competitive candidate in the field of multi-analyte detection and biosensing.

The proposed work has several limitations that can be addressed in the subsequent scope of research. For example the cross talk amongst the channels was not investigated. Furthermore, various losses such as insertion loss, attenuation loss, coupling loss, input-output loss etc. were not studied to keep the scope of the work limited. However, in future with a new scope these losses may be calculated which would further validate the credibility of this research work.

9.2 Scope of the Future Work

This research work used noble plasmonic material Au as the main material. In channel-2 and channel-3 over the Au layer Ta_2O_5 and TiO_2 were used respectively. Instead of Au, other materials may be used to look for performance improvement as a scope of future work. For example, Ag, Copper, Aluminium etc. may be used. As an overlayer Silicon Nitride (Si_3N_4) or graphene may be used. Furthermore, instead of traditional plasmonic material, alternative plasmonic material, for example, aluminum-doped zinc oxide, gallium doped zinc oxide, indium tin oxide, titanium nitride, etc may be used.

Future works may also be conducted by varying the design, design parameter, method of sensing (internal or combination of external and internal). In the case of variation in design, number of air-holes, air-hole size, value of pitch etc. may be explored to find enhanced results. This work is based on external sensing channel which is placed at the exterior of cladding. However, internal sensing channel may be explored to look for new results. Furthermore, combination of internal and external sensing channel may give more flexibility and it may increase capability of the sensor as the number of channels will increase. Additionally, internal and external sensing combination may widen the range of RI which would cover more variety of analyte.

List of Author's Publication

Journal Publications

[1] K. M. Mustafizur Rahman, M. Shah Alam, R. Ahmed, and M. Asiful Islam, "Irregular Hexagonal Core Based Surface Plasmon Resonance Sensor in Near-infrared Region," *Results in Physics*, p. 103983, 2021/02/25/ 2021, doi: <https://doi.org/10.1016/j.rinp.2021.103983>.

[2] K. M. M. Rahman, M. S. Alam, and M. A. Islam, "Highly Sensitive Surface Plasmon Resonance Refractive Index Multi-Channel Sensor for Multi-Analyte Sensing," *IEEE Sensors Journal*, vol. 21, no. 24, pp. 27422-27432, 2021, doi: [10.1109/JSEN.2021.3126624](https://doi.org/10.1109/JSEN.2021.3126624).

References

- [1] P. Bing *et al.*, "Analysis of Dual-Channel Simultaneous Detection of Photonic Crystal Fiber Sensors," *Plasmonics*, vol. 15, no. 4, pp. 1071-1076, 2020/08/01 2020, doi: 10.1007/s11468-020-01131-9.
- [2] N. D. Gómez-Cardona, E. Reyes-Vera, and P. Torres, "Multi-Plasmon Resonances in Microstructured Optical Fibers: Extending the Detection Range of SPR Sensors and a Multi-Analyte Sensing Technique," *IEEE Sensors Journal*, vol. 18, no. 18, pp. 7492-7498, 2018, doi: 10.1109/JSEN.2018.2861709.
- [3] A. Yasli, H. Ademgil, S. Haxha, and A. Aggoun, "Multi-Channel Photonic Crystal Fiber Based Surface Plasmon Resonance Sensor for Multi-Analyte Sensing," *IEEE Photonics Journal*, vol. 12, no. 1, pp. 1-15, 2020, doi: 10.1109/JPHOT.2019.2961110.
- [4] R. Otupiri, E. K. Akowuah, and S. Haxha, "Multi-channel SPR biosensor based on PCF for multi-analyte sensing applications," *Opt. Express*, vol. 23, no. 12, pp. 15716-15727, 2015/06/15 2015, doi: 10.1364/OE.23.015716.
- [5] V. Kaur and S. Singh, "A dual-channel surface plasmon resonance biosensor based on a photonic crystal fiber for multianalyte sensing," *Journal of Computational Electronics*, vol. 18, no. 1, pp. 319-328, 2019/03/01 2019, doi: 10.1007/s10825-019-01305-7.
- [6] M. F. Hameed, Y. K. Alrayk, A. Shaalan, W. El Deeb, and S. S. Obayya, "Design of highly sensitive multichannel bimetallic photonic crystal fiber biosensor," vol. 10 %J Journal of Nanophotonics, no. 4, p. 046016, 2016. [Online]. Available: <https://doi.org/10.1117/1.JNP.10.046016>.
- [7] F. Haider, R. Ahmmed Aoni, R. Ahmed, G. Amouzad Mahdiraji, M. Fahmi Azman, and F. R. M. Adikan, "Mode-multiplex plasmonic sensor for multi-analyte detection," *Opt. Lett.*, vol. 45, no. 14, pp. 3945-3948, 2020/07/15 2020, doi: 10.1364/OL.396340.
- [8] S. I. Azzam, M. F. O. Hameed, R. E. A. Shehata, A. M. Heikal, and S. S. A. Obayya, "Multichannel photonic crystal fiber surface plasmon resonance based sensor," *Optical and Quantum Electronics*, vol. 48, no. 2, p. 142, 2016/01/27 2016, doi: 10.1007/s11082-016-0414-4.
- [9] A. Yasli and H. Ademgil, "Multianalyte sensing analysis with multilayer photonic crystal fiber-based surface plasmon resonance sensor," *Modern Physics Letters B*, vol. 34, no. 33, p. 2050375, 2020, doi: 10.1142/s0217984920503753.
- [10] S. Roy, D. Ghosh, and S. Bhadra, *Guided Wave Optics and photonic devices* (Photonic Crystal Fibre: Basic Principles of Light Guidance, Fabrication Process and Applications). CRC Press, 2013.

- [11] R. J. A. P. S. A. Buczynski, "Photonic crystal fibers," vol. 106, no. 2, pp. 141-168, 2004.
- [12] A. A. Rifat, G. A. Mahdiraji, Y. M. Sua, R. Ahmed, Y. G. Shee, and F. R. M. Adikan, "Highly sensitive multi-core flat fiber surface plasmon resonance refractive index sensor," *Opt. Express*, vol. 24, no. 3, pp. 2485-2495, 2016/02/08 2016, doi: 10.1364/OE.24.002485.
- [13] Y. S. Kivshar and G. P. Agrawal, *Optical solitons: from fibers to photonic crystals*. Academic press, 2003.
- [14] B. Li, T. Cheng, J. Chen, and X. Yan, "Graphene-Enhanced Surface Plasmon Resonance Liquid Refractive Index Sensor Based on Photonic Crystal Fiber," *Sensors, MDPI*, vol. 19, no. 17, p. 3666, 2019. [Online]. Available: <https://www.mdpi.com/1424-8220/19/17/3666>.
- [15] W. Luo, X. Li, J. Meng, Y. Wang, and X. Hong, "Surface Plasmon Resonance Sensor Based on Side-Polished D-Shaped Photonic Crystal Fiber With Split Cladding Air Holes," *IEEE Transactions on Instrumentation and Measurement*, vol. 70, pp. 1-11, 2021, doi: 10.1109/TIM.2021.3054003.
- [16] S. Gafsi, "Highly nonlinear fiber characterization for mid-infrared applications," 2016.
- [17] M. Gerken and R. De La Rue, "Photonic Crystal Biosensors," in *Biomedical Optical Sensors: Differentiators for Winning Technologies*, R. De La Rue, H. P. Herzig, and M. Gerken Eds. Cham: Springer International Publishing, 2020, pp. 109-153.
- [18] S. O. Leonov, E. A. Yelistratova, V. V. Demidov, and A. D. Pryamikov, "Birefringence properties of anti-resonant octagonal-core and nodeless hollow-core fibers," *Appl. Opt.*, vol. 59, no. 16, pp. 5013-5019, 2020/06/01 2020, doi: 10.1364/AO.392175.
- [19] D. J. J. Hu and H. P. Ho, "Recent advances in plasmonic photonic crystal fibers: design, fabrication and applications," *Adv. Opt. Photon.*, vol. 9, no. 2, pp. 257-314, 2017/06/30 2017, doi: 10.1364/AOP.9.000257.
- [20] P. K. Maharana, P. Padhy, and R. Jha, "On the Field Enhancement and Performance of an Ultra-Stable SPR Biosensor Based on Graphene," *IEEE Photonics Technology Letters*, vol. 25, no. 22, pp. 2156-2159, 2013, doi: 10.1109/LPT.2013.2281453.
- [21] A. K. Sharma, R. Jha, and B. D. Gupta, "Fiber-Optic Sensors Based on Surface Plasmon Resonance: A Comprehensive Review," *IEEE Sensors Journal*, vol. 7, no. 8, pp. 1118-1129, 2007, doi: 10.1109/JSEN.2007.897946.
- [22] E. K. Akowuah, T. Gorman, and S. Haxha, "Design and optimization of a novel surface plasmon resonance biosensor based on Otto configuration," *Opt. Express*, vol. 17, no. 26, pp. 23511-23521, 2009/12/21 2009, doi: 10.1364/OE.17.023511.

- [23] Y. Xu *et al.*, "Optical Refractive Index Sensors with Plasmonic and Photonic Structures: Promising and Inconvenient Truth," vol. 7, no. 9, p. 1801433, 2019, doi: <https://doi.org/10.1002/adom.201801433>.
- [24] A. A. Rifat *et al.*, "Photonic crystal fiber based plasmonic sensors," *Sensors and Actuators B: Chemical*, vol. 243, pp. 311-325, 2017/05/01/ 2017, doi: <https://doi.org/10.1016/j.snb.2016.11.113>.
- [25] A. K. Sharma, A. K. Pandey, and B. Kaur, "A Review of advancements (2007–2017) in plasmonics-based optical fiber sensors," *Optical Fiber Technology*, vol. 43, pp. 20-34, 2018/07/01/ 2018, doi: <https://doi.org/10.1016/j.yofte.2018.03.008>.
- [26] L. C. Oliveira, A. M. N. Lima, C. Thirstrup, and H. F. Neff, "Physical Features of the Surface Plasmon Polariton," in *Surface Plasmon Resonance Sensors A Materials Guide to Design, Characterization, Optimization, and Usage*, 2nd Ed ed. Switzerland: Springer, 2019, ch. 70.
- [27] T. Allsop and R. Neal, "A Review: Evolution and Diversity of Optical Fibre Plasmonic Sensors," vol. 19, no. 22, p. 4874, 2019. [Online]. Available: <https://www.mdpi.com/1424-8220/19/22/4874>.
- [28] J. Homola, "Surface Plasmon Resonance Sensors for Detection of Chemical and Biological Species," *Chemical Reviews*, vol. 108, no. 2, pp. 462-493, 2008/02/01 2008, doi: 10.1021/cr068107d.
- [29] V. Kaur and S. Singh, "Design of D-Shaped PCF-SPR sensor with dual coating of ITO and ZnO conducting metal oxide," *Optik*, vol. 220, p. 165135, 2020/10/01/ 2020, doi: <https://doi.org/10.1016/j.ijleo.2020.165135>.
- [30] Y. Liu, S. Li, H. Chen, J. Li, W. Zhang, and M. Wang, "Surface Plasmon Resonance Induced High Sensitivity Temperature and Refractive Index Sensor Based on Evanescent Field Enhanced Photonic Crystal Fiber," *Journal of Lightwave Technology*, vol. 38, no. 4, pp. 919-928, 2020, doi: 10.1109/JLT.2019.2949067.
- [31] T. Li, L. Zhu, X. Yang, X. Lou, and L. Yu, "A Refractive Index Sensor Based on H-Shaped Photonic Crystal Fibers Coated with Ag-Graphene Layers," *Sensors*, vol. 20, no. 3, p. 741, 2020. [Online]. Available: <https://www.mdpi.com/1424-8220/20/3/741>.
- [32] J. Homola, H. B. Lu, G. G. Nenninger, J. Dostálek, and S. S. Yee, "A novel multichannel surface plasmon resonance biosensor," *Sensors and Actuators B: Chemical*, vol. 76, no. 1, pp. 403-410, 2001/06/01/ 2001, doi: [https://doi.org/10.1016/S0925-4005\(01\)00648-7](https://doi.org/10.1016/S0925-4005(01)00648-7).
- [33] C.-L. Tien, H.-Y. Lin, and S.-H. Su, "High Sensitivity Refractive Index Sensor by D-Shaped Fibers and Titanium Dioxide Nanofilm," *Advances in Condensed Matter Physics*, vol. 2018, p. 2303740, 2018/02/05 2018, doi: 10.1155/2018/2303740.

- [34] V. Kaur and S. Singh, "Performance analysis of multichannel surface plasmon resonance sensor with dual coating of conducting metal oxide," *Journal of Nanophotonics*, no. 1, p. 016012, 2018. [Online]. Available: <https://doi.org/10.1117/1.JNP.12.016012>.
- [35] A. Shakya and S. Singh, "Design and analysis of dual polarized Au and TiO₂-coated photonic crystal fiber surface plasmon resonance refractive index sensor: an extraneous sensing approach," vol. 15 %J *Journal of Nanophotonics*, no. 1, p. 016009, 2021. [Online]. Available: <https://doi.org/10.1117/1.JNP.15.016009>.
- [36] S. Singh and Y. K. Prajapati, "Highly sensitive refractive index sensor based on D-shaped PCF with gold-graphene layers on the polished surface," *Applied Physics A*, vol. 125, no. 6, p. 437, 2019/05/28 2019, doi: 10.1007/s00339-019-2731-5.
- [37] T. Wang *et al.*, "The effect of the TiO₂ film on the performance of the optical fiber SPR sensor," *Optics Communications*, vol. 448, pp. 93-97, 2019/10/01/ 2019, doi: <https://doi.org/10.1016/j.optcom.2019.05.023>.
- [38] M. A. A. Mamun, M. A. Islam, and M. S. Alam, "A square lattice photonic crystal fiber based surface plasmon resonance sensor with high sensitivity," in *2014 International Conference on Electrical Engineering and Information & Communication Technology*, 10-12 April 2014 2014, pp. 1-5, doi: 10.1109/ICEEICT.2014.6919108.
- [39] Y. Guo *et al.*, "Dual-polarized optical sensing of microstructure fiber with pentagonal-lattice based on surface plasmon resonance in the near-IR spectrum," *Optik*, vol. 202, p. 163671, 2020/02/01/ 2020, doi: <https://doi.org/10.1016/j.ijleo.2019.163671>.
- [40] B. D. Gupta, S. K. Srivastava, and R. Verma, *Fiber Optic Sensors based on Plasmonics* USA: World Scientific, 2015.
- [41] S. Zhang, J. Li, S. Li, Q. Liu, J. Wu, and Y. Guo, "Surface plasmon resonance sensor based on D-shaped photonic crystal fiber with two micro-openings," *Journal of Physics D: Applied Physics*, vol. 51, no. 30, p. 305104, 2018/07/06 2018, doi: 10.1088/1361-6463/aace72.
- [42] E. K. Akowuah, T. Gorman, H. Ademgil, S. Haxha, G. Robinson, and J. Oliver, "A Novel Compact Photonic Crystal Fibre Surface Plasmon Resonance Biosensor for an Aqueous Environment," in *Photonic Crystals –Innovative Systems, Lasers and Waveguides*, A. Massaro Ed. Croatia: InTech, 2012, ch. 6, p. 90.
- [43] Q. Liu *et al.*, "Surface plasmon resonance sensor based on photonic crystal fiber with indium tin oxide film," *Optical Materials*, vol. 102, p. 109800, 2020/04/01/ 2020, doi: <https://doi.org/10.1016/j.optmat.2020.109800>.
- [44] N. Chen, M. Chang, X. Zhang, J. Zhou, X. Lu, and S. Zhuang, "Highly Sensitive Plasmonic Sensor Based on a Dual-Side Polished Photonic Crystal Fiber for

- Component Content Sensing Applications," *Nanomaterials*, vol. 9, no. 11, p. 1587, 2019. [Online]. Available: <https://www.mdpi.com/2079-4991/9/11/1587>.
- [45] J. Wang *et al.*, "Surface plasmon resonance sensor based on coupling effects of dual photonic crystal fibers for low refractive indexes detection," *Results in Physics*, vol. 18, p. 103240, 2020/09/01/ 2020, doi: <https://doi.org/10.1016/j.rinp.2020.103240>.
- [46] Wikipedia. "List of refractive indices." https://en.wikipedia.org/wiki/List_of_refractive_indices (accessed 21 August 2021, 2021).
- [47] P. Y. Liu *et al.*, "Cell refractive index for cell biology and disease diagnosis: past, present and future," *Lab on a Chip*, 10.1039/C5LC01445J vol. 16, no. 4, pp. 634-644, 2016, doi: 10.1039/C5LC01445J.
- [48] A. N. Yaroslavsky *et al.*, "High-contrast mapping of basal cell carcinomas," *Opt. Lett.*, vol. 37, no. 4, pp. 644-646, 2012/02/15 2012, doi: 10.1364/OL.37.000644.
- [49] C. Tsai and S. Huang, "Water Distribution in Cancer and Normal Cells," ed: Accessed, 2012.
- [50] A. Yasli, "Cancer Detection with Surface Plasmon Resonance-Based Photonic Crystal Fiber Biosensor," *Plasmonics*, vol. 16, no. 5, pp. 1605-1612, 2021/10/01 2021, doi: 10.1007/s11468-021-01425-6.
- [51] N. Ayyanar, G. T. Raja, M. Sharma, and D. S. Kumar, "Photonic Crystal Fiber-Based Refractive Index Sensor for Early Detection of Cancer," *IEEE Sensors Journal*, vol. 18, no. 17, pp. 7093-7099, 2018, doi: 10.1109/JSEN.2018.2854375.
- [52] W. H. Reeves, J. C. Knight, P. S. J. Russell, and P. J. Roberts, "Demonstration of ultra-flattened dispersion in photonic crystal fibers," *Opt. Express*, vol. 10, no. 14, pp. 609-613, 2002/07/15 2002, doi: 10.1364/OE.10.000609.
- [53] R. F. Cregan *et al.*, "Single-Mode Photonic Band Gap Guidance of Light in Air," *Science*, vol. 285, no. 5433, pp. 1537-1539, 1999, doi: 10.1126/science.285.5433.1537.
- [54] R. T. Bise and D. J. Trevor, "Sol-gel Derived Microstructured Fiber: Fabrication and Characterization," in *Optical Fiber Communication Conference and Exposition and The National Fiber Optic Engineers Conference*, Anaheim, California, 2005/03/06 2005: Optical Society of America, in Technical Digest (CD), p. OWL6. [Online]. Available: <http://www.osapublishing.org/abstract.cfm?URI=OFC-2005-OWL6>. [Online]. Available: <http://www.osapublishing.org/abstract.cfm?URI=OFC-2005-OWL6>
- [55] Q. Coulombier *et al.*, *Fabrication of low losses chalcogenide photonic crystal fibers by molding process* (SPIE OPTO). SPIE, 2010.

- [56] Z. Guiyao, H. Zhiyun, L. Shuguang, and H. Lantian, "Fabrication of glass photonic crystal fibers with a die-cast process," *Appl. Opt.*, vol. 45, no. 18, pp. 4433-4436, 2006/06/20 2006, doi: 10.1364/AO.45.004433.
- [57] G. Amouzad Mahdiraji *et al.*, "Challenges and Solutions in Fabrication of Silica-Based Photonic Crystal Fibers: An Experimental Study," *Fiber and Integrated Optics*, vol. 33, no. 1-2, pp. 85-104, 2014/01/02 2014, doi: 10.1080/01468030.2013.879680.
- [58] H. Kim, J. Kim, U.-C. Paek, B. H. Lee, and K. T. Kim, "Tunable photonic crystal fiber coupler based on a side-polishing technique," *Opt. Lett.*, vol. 29, no. 11, pp. 1194-1196, 2004/06/01 2004, doi: 10.1364/OL.29.001194.
- [59] P. R. West, S. Ishii, G. V. Naik, N. K. Emani, V. M. Shalaev, and A. Boltasseva, "Searching for better plasmonic materials," *Laser & Photonics Review*, vol. 4, no. 6, pp. 795-808, 2010, doi: 10.1002/lpor.200900055.
- [60] A. Schwuchow *et al.*, "Monolayers of different metal nanoparticles in microstructured optical fibers with multiplex plasmonic properties," *Opt. Mater. Express*, vol. 2, no. 8, pp. 1050-1055, 2012/08/01 2012, doi: 10.1364/OME.2.001050.